catalysts

MDPI

Article

Synergistic Effect of NiAl-Layered Double Hydroxide and Cu-MOF for the Enhanced Photocatalytic Degradation of Methyl Orange and Antibacterial Properties

Iqra Batool [1,†], Sadia Aroob [1], Farheen Anwar [1,†], Muhammad Babar Taj [1,*], Doaa F. Baamer [2], Afaf Almasoudi [2], Omar Makram Ali [3], Reema H. Aldahiri [4], Fatimah Mohammad H. Alsulami [4], Muhammad Imran Khan [5,*], Aamir Nawaz [1], Ihsan Maseeh [1], Muhammad Khalid Nazir [6], Sónia A. C. Carabineiro [7], Abdallah Shanableh [5,8] and Javier Fernandez-Garcia [9,10]

[1] Institute of Chemistry, The Islamia University of Bahawalpur, Bahawalpur 63100, Pakistan; iqrab720@gmail.com (I.B.); sadiaaroob4991@gmail.com (S.A.); farheenanwar222@gmail.com (F.A.); aamirnawaz301@gmail.com (A.N.); ihsanullah1742@gmail.com (I.M.)
[2] Chemistry Department, Faculty of Science, King Abdulaziz University, P.O. Box 42734, Jeddah 21589, Saudi Arabia; dfbaamer@kau.edu.sa (D.F.B.); asalmasoudi@kau.edu.sa (A.A.)
[3] Department of Chemistry, Taraba University College, Taraba Branch, Taif University, P.O. Box 11099, Taif 21944, Saudi Arabia; om.ali@tu.edu.sa
[4] Department of Chemistry, College of Science, University of Jeddah, Jeddah 21959, Saudi Arabia; rhal-dhahery@uj.edu.sa (R.H.A.); fmal-sulami@uj.edu.sa (F.M.H.A.)
[5] Research Institute of Sciences and Engineering (RISE), University of Sharjah, Sharjah 27272, United Arab Emirates; shanableh@sharjah.ac.ae
[6] Institute of Chemical Sciences, Bahauddin Zakariya University, Multan 60800, Pakistan; khalidnazir82@gmail.com
[7] LAQV-REQUIMTE, Department of Chemistry, NOVA School of Science and Technology, Universidade NOVA de Lisboa, 2829-516 Caparica, Portugal; sonia.carabineiro@fct.unl.pt
[8] Scientific Research Center, Australian University, Mubarak Al-Abdullah 40250, Kuwait
[9] IQS School of Engineering, Universitat Ramon Llull, Via Augusta 390, 08017 Barcelona, Spain; javier.fernandez@iqs.url.edu
[10] Department of Chemical Engineering, University College London, Torrington Place, London WC1E 7JE, UK
* Correspondence: dr.taj@iub.edu.pk (M.B.T.); raoimranishaq@gmail.com (M.I.K.)
† These authors contributed equally to this work.

check for updates

Citation: Batool, I.; Aroob, S.; Anwar, F.; Taj, M.B.; Baamer, D.F.; Almasoudi, A.; Ali, O.M.; Aldahiri, R.H.; Alsulami, F.M.H.; Khan, M.I.; et al. Synergistic Effect of NiAl-Layered Double Hydroxide and Cu-MOF for the Enhanced Photocatalytic Degradation of Methyl Orange and Antibacterial Properties. *Catalysts* **2024**, *14*, 719. https://doi.org/10.3390/catal14100719

Academic Editor: Omid Akhavan

Received: 19 August 2024
Revised: 8 October 2024
Accepted: 9 October 2024
Published: 15 October 2024

Abstract: This study synthesized NiAl-layered double hydroxide (LDH)/Cu-MOF photocatalyst using a simple impregnation method involving NiAl-LDH and Cu-MOF. The successful synthesis was confirmed through Fourier transform infrared spectroscopy (FTIR), X-ray diffraction (XRD), scanning electron microscopy (SEM), zeta potential measurements, thermogravimetric analysis (TGA), ultraviolet diffuse reflectance spectroscopy (UV-DRS), N_2 adsorption at −196 °C, and electrochemical impedance spectroscopy (EIS). Photocatalysts based on NiAl-LDH, Cu-MOF, and NiAl-LDH/Cu-MOF were used to remove methyl orange (MO) dye from contaminated water. The impact of various factors, including pH, dye concentration, and photocatalyst amount, on MO degradation efficiency was assessed. FTIR analysis was conducted both before and after dye degradation. The optimal degradation conditions were a photocatalyst dose of 25 mg and a pH of 3. Kinetic studies indicated that the degradation of MO dye onto NiAl-LDH/Cu-MOF followed a pseudo-first-order and an L–H or Langmuir–Hinshelwood model. The value of $R^2 = 0.94$ confirms the validity of pseudo-first-order and Langmuir–Hinshelwood (L–H) kinetic models for the photocatalytic degradation of MO dye. This study highlights the importance of developing novel photocatalysts with improved degradation efficiency to protect the water environment. Antibacterial activity was also performed with antibacterial sensibility testing by disk diffusion to determine minimal inhibitory and bactericidal concentrations. In short, NiAl-LDH/Cu-MOF can be helpful for various biomedical and industrial applications.

Keywords: methyl orange; photocatalytic degradation; layered double hydroxide; metal–organic framework; water purification; antibacterial

1. Introduction

The main cause of water contamination is the excessive release of non-biodegradable, harmful dyes through effluents from different commercial sources, such as textile, leather, printing, food, and pharmaceutical industries, which affects aquatic life [1]. Due to the massive discharge of waste products, the environment has been severely contaminated, potentially leading to the deterioration of the ecosystem [2]. According to one report, more than 10^6 tons of dyestuff and colors are generated yearly [3]. Numerous methods, such as chemical, biological, and physical methods, have been used to remove harmful pollutants from the environment. While some techniques for breaking down pollutants have disadvantages, advanced oxidation processes (AOPs) have become a viable option because they are cost-effective and less time-consuming. These processes utilize semiconductors exposed to solar or ultraviolet (UV) light to create electron–hole pairs, which effectively break down dyes and other pollutants [4]. In other words, electrons excite the conduction band by imparting the valence or outermost band with holes (h^+) [5]. In other words, photocatalytic oxidation is widely recognized as a highly effective technique for breaking down dyes. Researchers are particularly interested in the photocatalytic deterioration of harmful pollutants because of its rapid processing speed, contamination prevention, efficiency, and hydroxyl radical (OH^-)-degrading properties in eliminating organic contaminants [6]. During photocatalysis, a suitable light energy is utilized to activate the catalyst particles to generate electron–hole pairs, which further yields very reactive radicals such as $O_2^{\bullet-}$ and OH species [7].

Recent research indicates that layered double hydroxides (LDHs) are recognized as cost-effective, environmentally sustainable, and readily accessible catalysts for efficiently removing pollutants from water sources [8]. LDHs (termed as hydrotalcite) or anionic clays have the basic formula $M(II)_{1-x}\ M(III)_X\ (OH)_2\ (A^{n-})_{x/n} \times yH_2O$, where M(II) and M(III) represent the divalent and trivalent metal cations, respectively, A^{n-} is the interlayer anion, and x is the molar fraction of the trivalent cations (M(III)) [9,10]. The vast surface areas, layered structure, and strong ion exchange capabilities of LDHs make them effective photocatalysts for pollutant deterioration [11]. Similarly, nanoscale porous materials are widely employed in various environmental protection activities, such as removing dyes from the environment.

Porous materials, also called coordination polymers or metal–organic frameworks (MOFs), have attracted significant interest because of their extensive surface area, increased stability, customizable pore size, available metal sites, and orderly crystalline structure [10,12,13]. MOFs have metals linked to the organic linker or ligand by a strong coordination bond. Owing to their structural stability and properties, such as large surface area, controllable function and structure, and accessible active sites, MOFs have gained tremendous attention in photocatalysis. They can be utilized as alternative photocatalysts for deteriorating pollutants from the wastewater environment [14]. In many studies, Cu-MOFs have been employed as efficient photocatalysts because of their large area of the outermost layer and high permeability [15]. Recent research on dye degradation has used only LDHs or MOFs, but no research has been reported using their composites. LDHs are significant building blocks for manufacturing LDH–metal composites because the metal atoms on their surface have linkage sites that serve as activation areas for directed epitaxial growth and nucleation [16]. Separately, MOFs and LDHs are not considered effective photocatalysts for the deterioration of harmful pollutants due to significant bandgaps, poor water stability, and less charge separation [17]. The combination of NiAl LDH's ability to generate ROS and Cu-MOF's efficient light absorption and electron transfer can lead to a more effective photocatalytic system. The structural stability of NiAl LDH can help maintain the strength of the overall photocatalytic system. Cu-MOF simultaneously contributes to a sizeable uppermost layer area and improves light absorption. The complementary properties of NiAl LDH and Cu-MOF might enable the photocatalyst to work efficiently under a broader spectrum of light and for a more comprehensive range of dyes. Ghayah M. Alsulaim synthesized $BaTi_{0.96}Cu_{0.02}X_{0.02}O_3$ (X = V, Nb) photocatalyst for the degradation of methyl blue and methyl green dye under sunlight and xenon lamp irradiation and achieved 94% and 97% efficiency within 90 and 60 min, respectively [7]. The fabrication and design of highly active photocatalysts for achieving desirable and efficient removal of pollutants are necessary; therefore, here, in this study, the NiAl LDH/Cu-MOF composite is expected to represent a powerful approach for the photocatalytic degradation of pollutants due to their combined benefits of high outer layer area, efficient light absorption, and strong redox capabilities. This makes them promising candidates for environmental remediation applications, particularly in treating wastewater containing organic dyes.

So, in this study, the NiAl-LDH/Cu-MOF composite was prepared directly from NiAl-LDH and Cu-MOF using a thermal impregnation method. We conducted a combined analysis of the effects of the NiAl-LDH/Cu-MOF composite with significant photocatalytic and light-harvesting properties. As a result, the comparative potential of NiAl-LDH/Cu-MOF was studied to degrade MO dye. The % removal of MO dye for each prepared photocatalyst was conducted using an ultraviolet–visible spectrometer. The impact of pH, catalyst amount, dye quantity, process time, and the effect of H_2O_2 on MO degradation was studied. Kinetics models were utilized to analyze the mechanisms involved in photocatalytic degradation. Additionally, the reusability of NiAl-LDH/Cu-MOF was assessed to determine its potential for cost-effective photodegradation. Antibacterial activity was also performed with antibacterial sensibility testing by disk diffusion to calculate minimal inhibitory concentration (MIC) and minimum bactericidal concentration (MBC). The high antibacterial potential of NiAl-LDH/Cu-MOF is due to its narrow bandgap.

A narrow bandgap increases a photocatalyst's antibacterial activity by allowing it to absorb more light, generate more reactive oxygen species, and separate charge carriers more efficiently [18]. These factors collectively enhance the photocatalyst's ability to destroy microorganisms effectively, especially when exposed to light sources, including visible light [19]. Such photocatalysts can be incorporated into coatings for surfaces in hospitals, public spaces, or homes to provide self-cleaning and antibacterial properties [20].

2. Results and Discussion

2.1. FTIR Analysis

FTIR is the best and most effective method for detecting functional groups in the sample. Figure 1 shows Cu-MOF spectra, where the vibrational bands at 1396 cm^{-1} and 1596 cm^{-1} correspond to COOH-asymmetric and -symmetric stretching coordination from terephthalic acid (BDC), respectively. The vibrational frequencies at 734 cm^{-1} and 1020 cm^{-1} are narrow and weak, indicating the C-H bending (δ) and C-H stretching (γ) vibrations of aromatic rings present in BDC, respectively [21,22]. These peaks signify the presence of the organic ligand in the sample. The phenyl ring vibrations are evidenced by 1505 cm^{-1} and 775 cm^{-1} bands. The aliphatic C-H asymmetric stretching vibrations of dimethylformamide are attributed to the peak at 2924 cm^{-1} [15]. The band in the 3400–3600 cm^{-1} range is due to the hydroxyl group present in carboxylic acids or maybe due to crystallized water.

The presence of a broad band at 3300–3600 cm^{-1} is attributed to water in the sheets of NiAl-LDH or the stretching frequencies of the -OH groups in the LDH layers. A smaller vibrational stretch at 1630 cm^{-1} is due to H_2O molecules bending regions in the interlayers of NiAl-LDH [23]. The spectrum of LDH primarily consists of three regions: a band at 1400 cm^{-1} indicating the vibrations of NO_3^- ions in the interlayers, a weak band at 1600 cm^{-1} showing carbonate anions acting as interlayer anions, and small bands at 810 cm^{-1}, 671 cm^{-1}, and 433 cm^{-1} corresponding to metal vibrations, such as M-O and M-OH vibrations within the LDH lattice [24].

The peak in the 3000 cm^{-1} to 3600 cm^{-1} range is due to the vibrational stretching of the -OH groups present in the LDH sheets and the H_2O molecules in the interlayers of LDH. The bands observed at 1580 cm^{-1} and 1428 cm^{-1} correspond to the asymmetric and symmetric vibrations of the OCO^- groups in the NiAl-LDH/Cu-MOF photocatalyst. The peak at 867 cm^{-1} is associated with the stretching frequencies of nitrate ions. The vibrational bands below 750 cm^{-1} are due to metal vibrations, either with oxygen or hydroxyl groups.

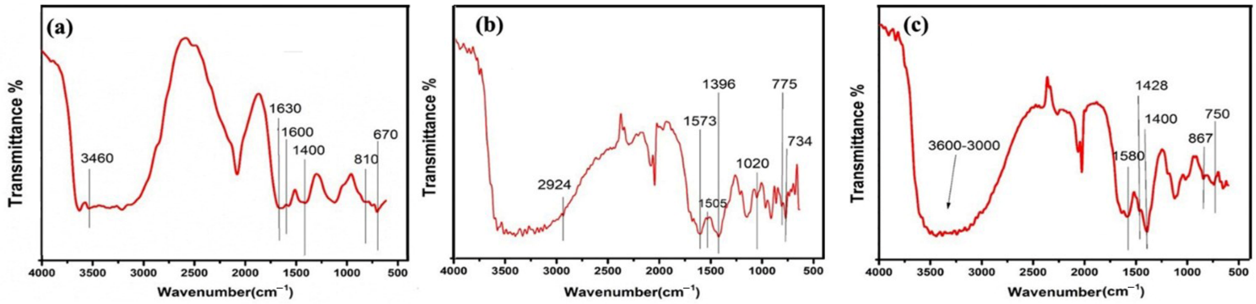

Figure 1. FTIR spectra of (**a**) NiAl-LDH, (**b**) Cu-MOF, and (**c**) NiAl-LDH/Cu-MOF composite.

2.2. PXRD Analysis

Figure 2 represents the XRD pattern of NiAl-LDH, Cu-MOF, and NiAl-LDH/Cu-MOF composite catalyst samples; the distinct reflections of all three samples are given below. Specifically, for NiAl-LDH, the peaks observed at 2θ of 11.6°, 24.3°, 32.2°, 46.2°, and 58.7° correspond to (003), (006), (012), (015), and (018) planes, which is well in agreement with the NiAl-LDH crystal structure reported in PDF# 15-0087 [25–27]. Further, there is a doublet of (110)–(113) planes within the 2θ range of 60–62° that corresponds to the typical hydrotalcite-like LDH reflections without other crystalline phases. Also in parallel with the works of others [28–34], the Cu-MOF is characterized by its layer stacking direction, as the prominent reflections of the (20-1) and (40-2) planes show that these planes are not parallel to the direction of layer organizing; the flat upper and lower surfaces are bounded by (20-1) facets [35,36]. Based on Figure 2, it is concluded that the XRD graph of NiAl-LDH, Cu-MOF, and NiAl-LDH/Cu-MOF composite have distinguishable similarities in terms of layered crystal structure. These broad peaks might be due to significant interactions between Cu-MOF and NiAl-LDH.

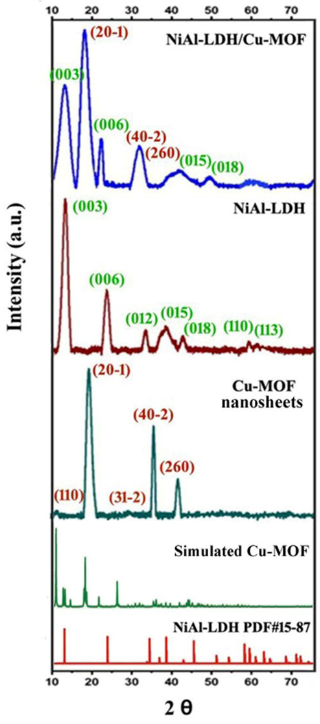

Figure 2. PXRD patterns of Cu-MOF, NiAl-LDH, and NiAl-LDH/Cu-MOF composite.

It was also found quantitatively that the crystallite size was about 41.23 nm using the Debye–Scherrer formula:

$$D = k\lambda/\beta cos\theta \tag{1}$$

The crystallite size in nm is represented by D; k is Scherrer's constant equal to 0.98; FWHM is, and θ is Bragg's angle.

2.3. Morphology Analysis

Figure 3 shows an SEM image surface displaying the morphology of NiAl-LDH, Cu-MOF, and NiAl-LDH/Cu-MOF composite. Cu-MOF grains are present as small aggregates on the NiAl-LDH layers. The -OH groups on NiAl-LDH sheet's surface facilitate the directed attachment of Cu-MOF through heterogeneous nucleation, leading to the organized growth of individual Cu-MOF grains on the NiAl-LDH surface of the adsorbent [37]. Additionally, the positively charged metal sites on the NiAl-LDH surface can provide binding sites for in situ nucleation and guide the growth of Cu-MOFs due to their unsaturated coordination state [38].

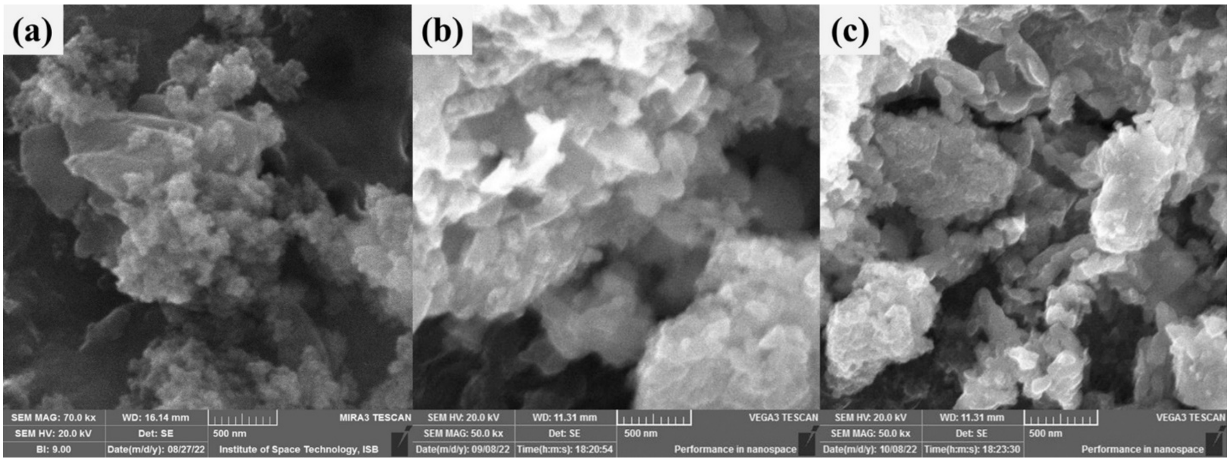

Figure 3. SEM images of (**a**) NiAl-LDH, (**b**) Cu-MOF, and (**c**) NiAl-LDH/Cu-MOF composite.

2.4. Zeta Potential

Zeta potential measurement is an essential technique for characterizing catalysts, as it determines the surface charge of a solid sample to its surrounding liquid and helps understand the physical stability of nanosuspensions. Zeta potential, known as the electrostatic double layer, is measured in millivolts (mVs). The zeta potential's magnitude shows how much electrostatic repulsion or attraction exists between particles with similar charges in dispersion. A high absolute value of zeta potential, whether positive or negative, indicates electrostatic interactions that help maintain high physical stability. Zeta potential values usually fall between +100 mV and −100 mV, with values beyond the range of −30 mV to +30 mV generally indicating sufficient electrostatic force to uphold physical stability in colloidal systems. These values were measured at different applied voltages to investigate the stability of NiAl-LDH, Cu-MOF, and NiAl-LDH/Cu-MOF catalysts, as shown in Figure 4a. The results obtained were 15.20 mV for NiAl-LDH, −8.75 mV for Cu-MOF, and 1.0 mV for the NiAl-LDH/Cu-MOF composite. Zeta potential values range between −10 and +10 mV and are considered neutral. Particles are classified as strongly cationic or anionic if the zeta potential is larger than +30 mV or less than −30 mV. At pH values above 4, deprotonation of the COOH groups on the BTC ligand causes the Cu-MOF surface to become negatively charged at pH 7.4 [39]. The zeta potential value of 1.0 mV for the NiAl-LDH/Cu-MOF composite indicates strong interactions between NiAl-LDH and Cu-MOF.

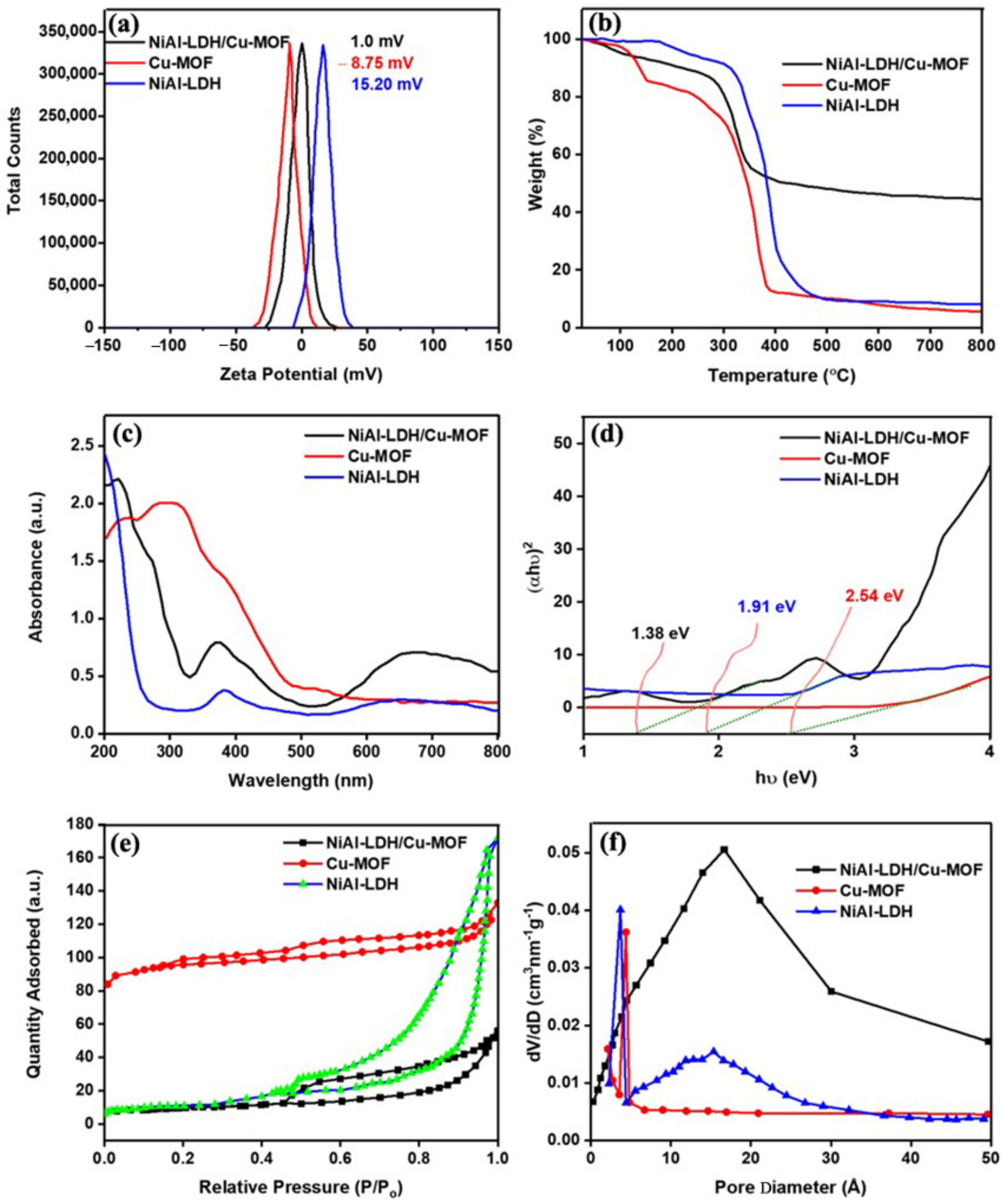

Figure 4. (**a**) Zeta potential, (**b**) TGA, (**c**) DRS, (**d**) Tauc plot, (**e**) N_2 adsorption–desorption isotherm, and (**f**) BJH pore size of NiAl-LDH/Cu-MOF composite, Cu-MOF, and NiAl-LDH catalysts.

2.5. Thermogravimetric Analysis

TGA measures how a material's mass changes with temperature, helping to determine its thermal stability. For LDH/MOF composites, understanding how these materials decompose or lose mass at elevated temperatures is crucial for assessing their suitability for various applications, particularly those involving high temperatures. TGA can provide insights into the interactions between LDH and MOF components. Changes in the thermal decomposition profile might indicate the formation of some new bonds or interactions at the interface of the two materials, which can affect the overall properties of the composite.

Figure 4b shows the TG plot of Cu-MOF, which exhibits three distinct weight loss stages. The initial stage, occurring below 200 °C, corresponds to chemically or physically absorbed H_2O loss. The second stage, characterized by significant weight loss between 300 °C and 400 °C, indicates the primary thermal decomposition of Cu-MOF. Above 420 °C, the third stage shows Cu-O formation as a degradation byproduct [40].

In the TGA measurements of NiAl-LDH, the weight decrease from 100 °C to 350 °C is attributed to the evaporation of water from both the internal surface and adsorbed molecules [41]. The second event, between 210 °C and 450 °C, is related to the breakdown of hydroxide layers and anions in interlamellar space. This leads to the decomposition of the layered structure's NO_3^- ions and concurrent oxide crystallization [42].

The TGA curve of NiAl-LDH/Cu-MOF integrates features from both NiAl-LDH and Cu-MOF curves. The weight loss from 30 °C to 300 °C is assigned to the dehydration of the material. The second event, between 300 °C and 400 °C, results from the evaporation of water during the dehydroxylation of NiAl-LDH layers and the degradation of intercalated Cu-MOF. The high residue formation indicates successful attachment of MOF to NiAl-LDH as fillers, enhancing its thermal stability [43].

2.6. UV–Vis DRS Analysis

Ultraviolet-visible diffused reflection spectroscopy (DRS) analysis (Figure 4c,d) was performed to investigate the NiAl-LDH/Cu-MOF composite synthesis from NiAl-LDH and Cu-MOF. Additionally, the bandgap value was estimated using Tauc's plot equation.

$$\alpha hv = A\left(E_g - hv\right)^2 \quad (2)$$

where α is the absorption coefficient, hv is the photon source, A is the constant of proportionality, and E_g is the energy gap [44]. The results show that the bandgap values of NiAl-LDH (1.91 eV) and Cu-MOF (2.54 eV) are reduced to 1.38 eV in the NiAl-LDH/Cu-MOF catalyst, confirming the successful synthesis of the material.

The Tauc plot is used to estimate the optical bandgap of materials. Bandgap energy is a crucial factor in determining photocatalytic efficiency for photocatalysts [45]. A material's ability to degrade dyes depends significantly on its bandgap, which dictates the energy required to generate charge carriers to drive the degradation process [46]. By plotting $(\alpha hv)^n$ versus hv, the Tauc plot helps identify the bandgap energy. This information is used to optimize the photocatalytic properties of catalysts, ensuring they have the proper bandgap to absorb sufficient light and effectively degrade dyes. The Tauc plot is vital in dye degradation studies because it directly impacts the photocatalytic activity and overall effectiveness of the material in degrading dyes [47].

2.7. N_2 Adsorption–Desorption Isotherm

N_2 adsorption–desorption isotherms provide comprehensive information about photocatalysts' porous structure and surface area. These data are crucial for understanding their potential applications, optimizing their performance, and ensuring the consistency and quality of the material. NiAl-LDH, Cu-MOF, and NiAl-LDH/Cu-MOF composite adsorption isotherms are classified as type IV, indicating capillary condensation behavior. The Brunauer–Emmett–Teller (BET) specific surface areas are 15 m^2/g for NiAl-LDH, 312.5 m^2/g for Cu-MOF, and 25 m^2/g for NiAl-LDH/Cu-MOF composite. The lower specific surface area of NiAl-LDH/Cu-MOF compared to Cu-MOF may be attributed to the pulverization effect during the thermal impregnation process. Increased temperatures could have destroyed some pores, and internal atoms might have occupied numerous empty spaces within NiAl-LDH/Cu-MOF, thus reducing the specific outermost layer area. Figure 4f presents the pore size distributions of NiAl-LDH, Cu-MOF, and NiAl-LDH/Cu-MOF composite, as measured using the Barrett–Joyner–Halenda (BJH) method from the desorption branches of N_2 adsorption–desorption isotherms. The most probable pore diameters are 16.05 nm for NiAl-LDH, 6.05 nm for Cu-MOF, and 19.02 nm for NiAl-

LDH/Cu-MOF. All these values fall within the mesopore range (2–50 nm). The increase in pore size for NiAl-LDH/Cu-MOF suggests a mesoporous structure that provides numerous active sites, potentially enhancing the degradation of the MO dye.

2.8. Reaction Mechanism of NiAl-LDH/Cu-MOF

The EIS curve at the contact interface reflects the working material's charge transfer rate and the electrolyte solution. In general, lower resistance leads to a smaller radius for charge transfer [48]. In Figure 5a, the radius corresponding to the Nyquist circle of the above sample is NiAl-LDH > Cu-MOF > NiAl-LDH/Cu-MOF. In conclusion, the NiAl-LDH/Cu-MOF combination not only accelerates the separation of carriers by applying the p-n junction built-in electric field but also constructs efficient channels for electron transport to accelerate the transfer of electrons and improve the ability to capture charge.

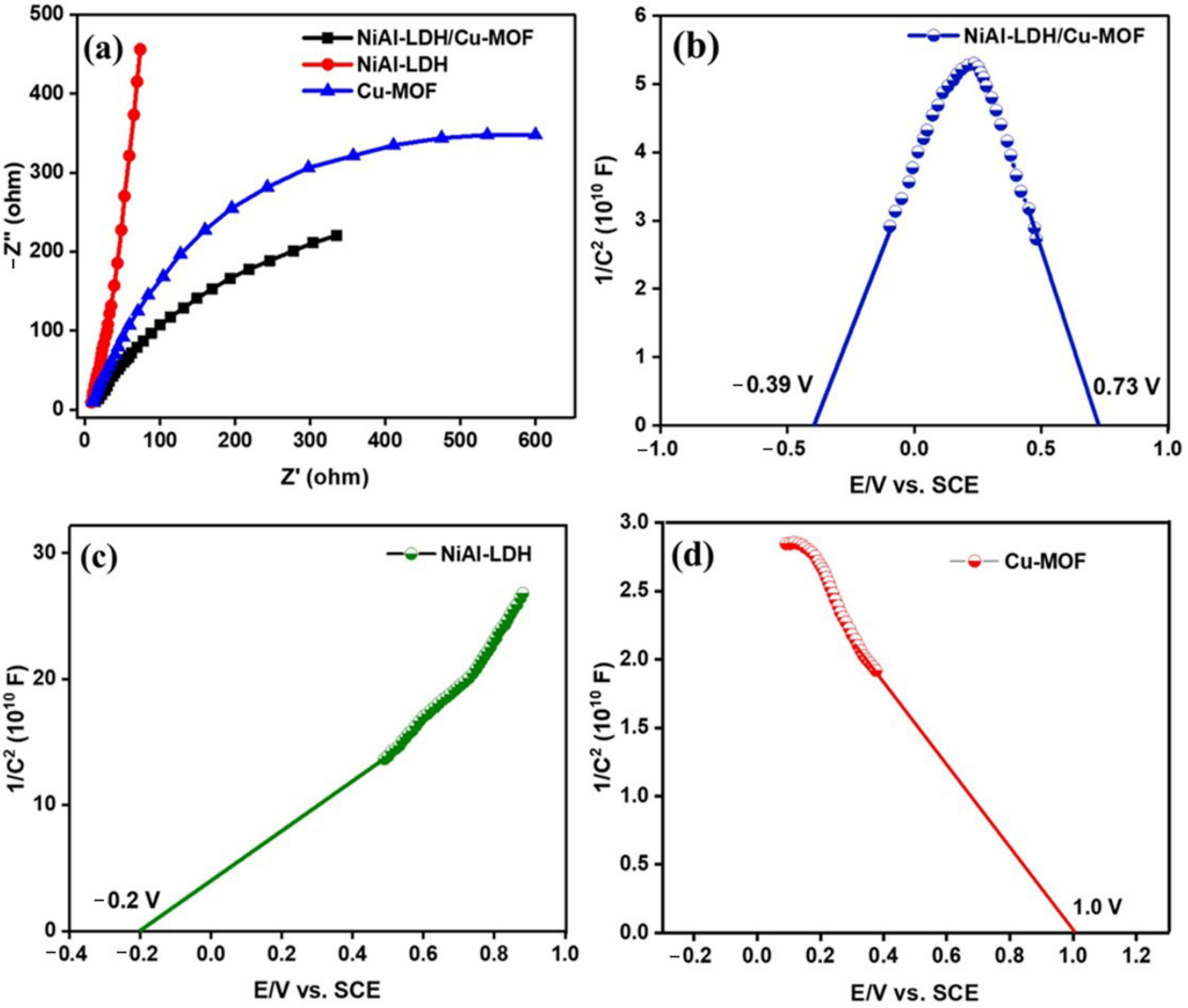

Figure 5. (**a**) The EIS curves of NiAl-LDH/Cu-MOF, NiAl-LDH, and Cu-MOF and (**b**–**d**) Mott–Schottky plots of NiAl-LDH/Cu-MOF, NiAl-LDH, and Cu-MOF.

For a better understanding of the photocatalytic activity of the NiAl-LDH/Cu-MOF, we studied the conduction and valence band positions of NiAl-LDH and Cu-MOF. The flat band potentials of n-type NiAl-LDH and p-type Cu-MOF were estimated by the Mott–Schottky (M–S) as −0.2 V and 1.0 V, respectively. Previous studies have shown that n-type semiconductor conduction band potential (ECB) is more negative than 0.2 [49] than the Fermi level at the interface (Efb), and p-type semiconductor valence band potential (EVB) is more positive at 0.2 than the Efb [50]. Therefore, the ECB of NiAl-LDH is estimated to be −0.4 V versus Saturated Calomel Electrode (SCE). Correspondingly, the EVB of Cu-MOF is 1.2 V versus SCE. The EVB of NiAl-LDH and the ECB of Cu-MOF were determined from UV–Vis/DRS (Figure 4d) and M–S techniques (Figure 5b,c) by the equation given as follows:

$$E_{VB} = E_{CB} + E_g \tag{3}$$

Notably, the M–S findings provided substantial evidence to clarify the mechanism of electron transfer discussed in this study. The EVB of NiAl-LDH and ECB of Cu-MOF were calculated as 1.51 V and −1.34 V, respectively. The successful construction of the NiAl-LDH/Cu-MOF p-n heterojunction can also be confirmed by the "V-shaped" Mott–Schottky diagram [27], as shown in Figure 5b. More importantly, in comparison with Cu-MOF, NiAl-LDH/Cu-MOF showcases a negative shift in flat band potential (1.0 → 0.73 V), which illuminates the upward shifting of Fermi levels of p-type Cu-MOF. Based on the above analysis, it can be concluded that the construction of the NiAl-LDH/Cu-MOF combination was successful.

2.9. Mechanism of Deterioration of MO Dye

The deterioration process of MO in an aqueous solution is influenced by the surface charge of the prepared NiAl-LDH/Cu-MOF composite and the dye molecules, which in turn depend on the pH values. The particles carry a positive and negative charge below and above the isoelectric point (IEP). In acidic and basic mediums, the surface charge on the photocatalyst becomes positive and negative, respectively. In other words, the solution's pH is crucial in determining the charge distribution on the particle surfaces. Thus, there is an interplay between the photocatalyst and the dye molecules, which is also influenced by changes in pH.

Figure 6 illustrates the electronic band structure and charge transfer mechanism of the NiAl-LDH/Cu-MOF composite, which depends on the band potentials of NiAl-LDH and Cu-MOF (1.38 eV, 1.91 eV, and 2.54 eV, respectively). Upon light irradiation, electron–hole pairs are generated in both NiAl-LDH and Cu-MOF. The separation and transfer of these photoexcited charges occur due to the difference in the band edge positions of the two materials [51]. The conduction band (C.B.) of Cu-MOF is lower than the C.B. of NiAl-LDH, while the valence band (V.B.) of NiAl-LDH is higher than the V.B. of Cu-MOF. This band alignment facilitates the transfer of excited electrons from the C.B. of NiAl-LDH to the C.B. of Cu-MOF, reducing the recombination rate of electron–hole pairs. Simultaneously, holes in the V.B. of Cu-MOF can recombine with electrons in the V.B. of NiAl-LDH, further enhancing charge separation [52].

This efficient separation of charges leads to the generation of reactive species such as superoxide radicals (dioxygen anions, $O_2^{\bullet -}$), hydroxyl radicals (·OH), and holes (h^+), which are responsible for the photodegradation of pollutants. Specifically, the photogenerated electrons from NiAl-LDH's conduction band can reduce O_2 to form superoxide radicals (dioxygen anions, $O_2^{\bullet -}$), while holes from the valence band of Cu-MOF can oxidize H_2O to form hydroxyl radicals (·OH) [53].

Under sunlight irradiation, the electrons in the conduction band of NiAl-LDH are transferred to Cu-MOF, while the holes left in the V.B. of Cu-MOF participate in oxidation reactions. The proposed photocatalytic reactions can be described as follows:

$$Photocatalyst + hv \rightarrow e^-_{C.B} + h^+_{V.B} \tag{4}$$

$$\mathrm{H_2O} + h^+_{V.B} \rightarrow \mathrm{OH^{\cdot}} + \mathrm{H^+} \tag{5}$$

$$e^-_{C.B} + \mathrm{O_2} \rightarrow \left[\mathrm{O_2^-}\right] \tag{6}$$

$$\mathrm{H^+} + \left[\mathrm{O_2^-}\right] \rightarrow \mathrm{HO_2^{\cdot}} \tag{7}$$

$$2\mathrm{HO_2^{\cdot}} \rightarrow \mathrm{H_2O_2} + \mathrm{O_2} \tag{8}$$

$$H_2O_2 \rightarrow 2\ OH^{\cdot} \quad (9)$$

$$\text{MO Dye} + OH^{\cdot} \rightarrow H_2O + CO_2 \quad (10)$$

Equation (4) shows that upon light irradiation, the electrons are excited from the valence band (V.B.) to the conduction band (C.B.), leaving behind holes. The holes in the valence band react with water molecules, generating hydroxyl radicals (·OH), which are highly reactive (Equation (5)). The electrons in the conduction band reduce oxygen molecules, forming superoxide anions ($O_2\bullet^-$), as in Equation (6). Protons from the solution react with superoxide anions to form hydroperoxyl radicals ($HO_2\bullet$), as depicted in Equation (7). Hydroperoxyl radicals react to produce hydrogen peroxide (H_2O_2) and oxygen (Equation (8)). Hydrogen peroxide decomposes into two hydroxyl radicals (Equation (9)). The MO dye molecules are oxidized by hydroxyl radicals and degraded into harmless products such as CO_2 and H_2O (Equation (10)).

The proposed mechanism demonstrates that the NiAl-LDH/Cu-MOF composite efficiently separates the photoexcited electron–hole pairs, leading to enhanced generation of reactive oxygen species (ROS) and thus improving the photodegradation of MO dye. Figure 6 provides a diagrammatic representation of this process.

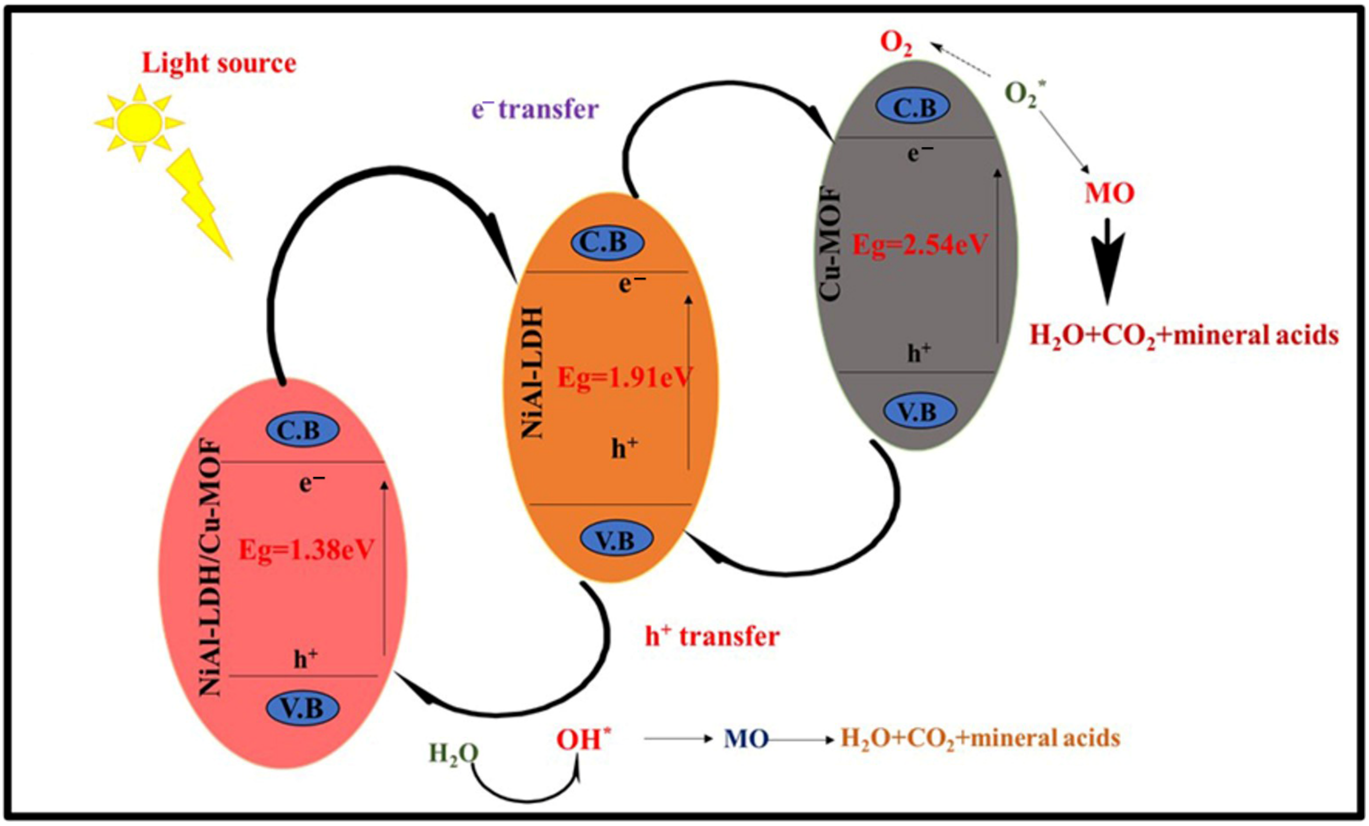

Figure 6. Mechanistic representation of MO dye degradation by the NiAl-LDH/Cu-MOF composite.

2.10. Factors Affecting Degradation Efficiency of MO

2.10.1. Effect of Contact Time

The effect of process time on MO dye removal from aqueous solution using NiAl-LDH, Cu-MOF, and NiAl-LDH/Cu-MOF composite was examined using UV–VIS spectroscopy at pH 3 with 25 mg concentration of NiAl-LDH, Cu-MOF, and NiAl-LDH/Cu-MOF composite and 5 ppm dye concentration, as shown in Figure 7a–c. The NiAl-LDH/Cu-MOF photocatalyst demonstrated a 99% degradation efficiency within 80 min, with a catalytic amount of 25 mg and a dye concentration of 5 ppm in 30 mL. Under the same conditions, NiAl-LDH exhibited a 94% removal efficiency, while Cu-MOF showed 82% removal efficiency. The degradation of MO dye was remarkably swifted for NiAl-LDH/Cu-MOF and a little less for NiAl-LDH and Cu-MOF compared to NiAl-LDH/Cu-MOF within 80 min. This high increase in degradation rate with time is assigned to the abundant activation sites on the catalytic materials readily interacting with the dye [54].

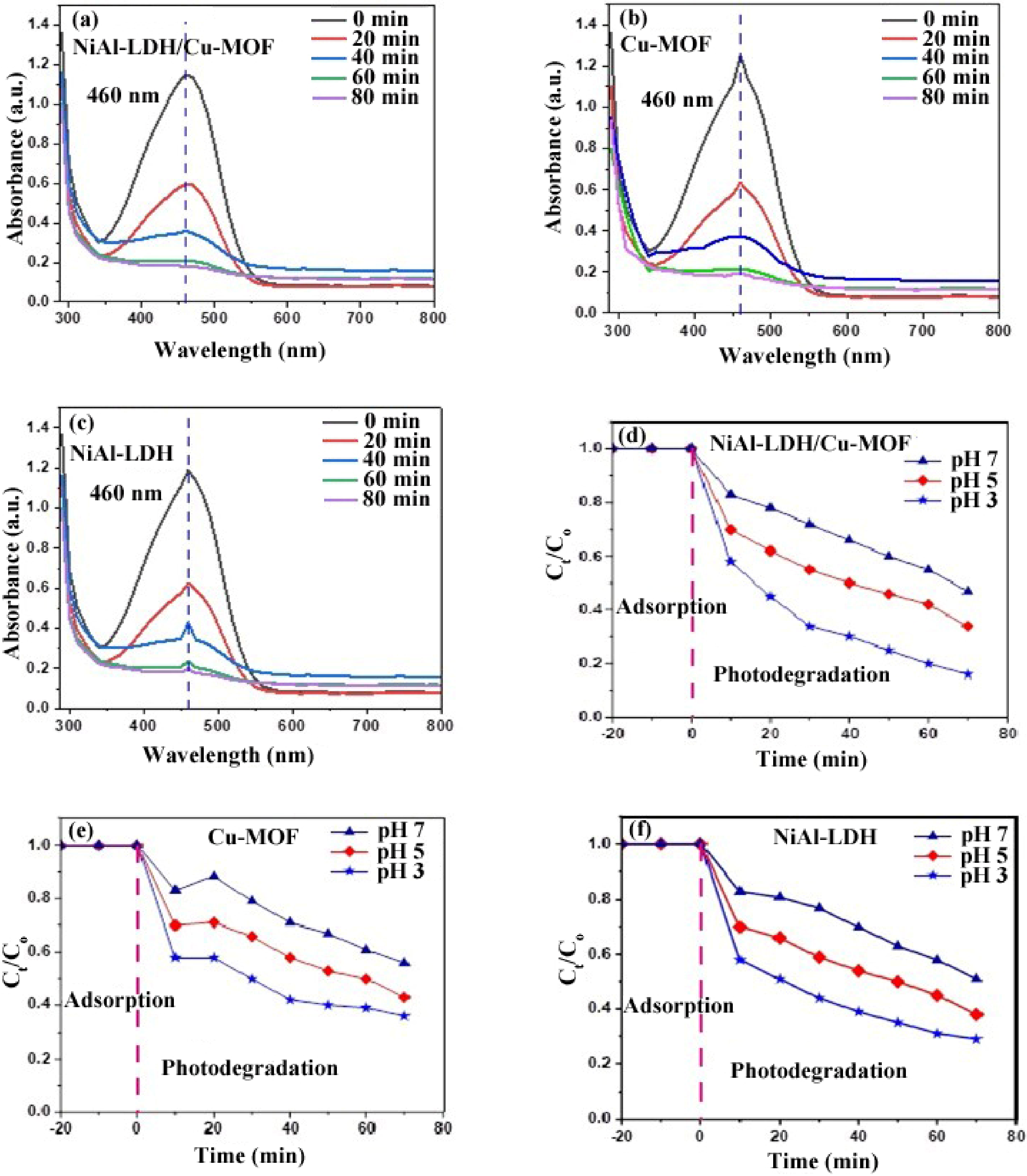

Figure 7. (**a**–**c**) UV–Vis spectra showing the degradation of MO dye by NiAl-LDH/Cu-MOF, Cu-MOF, and NiAl-LDH and (**d**–**f**) photocatalytic degradation of MO at pH 3, 5, and 7 by NiAl-LDH/Cu-MOF, Cu-MOF, and NiAl-LDH.

2.10.2. pH Effect

The pH affects the performance of photocatalysts as it influences their surface structure and chemistry [55]. This impact is mainly due to the charge on the photocatalyst and the ionic chemistry of the solution. Removal efficiencies of NiAl-LDH/Cu-MOF, Cu-MOF, and NiAl-LDH were examined at various pH values 3, 5, and 7, as shown in Figure 7d–f. In the dark or before sunlight irradiation, no changes were found in the dye with change in pH after the addition of the NiAl-LDH/Cu-MOF composite, Cu-MOF, and NiAl-LDH and the color of the dye does not change, which means that adsorption efficiency is very low or almost zero [56]. The highest deterioration efficiency for all three composites was observed at pH 3 [57,58]. But when exposed to sunlight, NiAl-LDH/Cu-MOF exhibit excellent degradation of MO dye, which can be attributed to the strong electrostatic interaction between the anionic MO dye and the cationic NiAl-LDH/Cu-MOF composite surface [22,37,59]. As the pH increases toward basic conditions, degradation decreases due to competition between hydroxyl groups and the sulfonate groups of the MO dye for sites for binding on the cationic NiAl-LDH/Cu-MOF composite [8]. Additionally, at a higher pH, electrostatic repulsion between the anionic dye molecules and the negatively charged upper layer, due to increased OH^- ions on the NiAl-LDH/Cu-MOF surface, should also be considered [38,60]. Cu-MOF also showed higher removal efficiency at pH 3, which may be due to its surface charge becoming positive, facilitating interaction with the anionic MO dye through mechanisms such as electrostatic attraction [15,22]. The prepared catalyst absorbs H^+ in an acidic medium, producing a high positive charge that effectively degrades MO dye.

2.10.3. Initial Dye Concentration Effect

The dye dosage influences the photocatalyst surface's active sites, affecting the degradation potential. As the initial dye amount enhances, the sites become more saturated with dye molecules, causing a decrease in the degradation process. The amount of MO dye plays a crucial role in achieving optimal removal efficiency, depending on the dose, pH, and process time. It also impacts the overall degradation efficiency.

In the experiment, the photocatalyst dose was fixed at 25 mg. The dye concentration was 5, 10, 15, and 20 ppm, maintaining a constant time of 80 min, as shown in Figure 8a–c. In the dark or before sunlight irradiation, no changes were found in MO dye concentration after the addition of the NiAl-LDH/Cu-MOF composite, Cu-MOF, and NiAl-LDH and the color of the dye does not change, which means that adsorption efficiency is very low or almost zero [56]. However, after irradiation with sunlight, the NiAl-LDH/Cu-MOF composite exhibits maximum degradation efficiency compared to Cu-MOF and NiAl-LDH at 5 ppm MO dye concentration. Degradation efficiency decreased with increasing dye dosage, which may be attributed to a reduction in the number of available sites on the photocatalyst for MO dye degradation [61]. This decrease in degradation efficiency with higher dye concentrations could also be attributed to more dye particles competing for the limited sites [62].

At high MO dye concentrations, dye removal efficiency is reduced because insufficient free active sites accommodate all the MO particles. The amount of dye initially used impacts the efficiency of photocatalytic degradation because it is linked to the number of active sites on the surface of the photocatalyst. When the dye dosage is increased, the effectiveness of removal is decreased, possibly because of the higher amount of intermediates and the absorption of sunlight by the MO dye in comparison to the NiAl-LDH/Cu-MOF composite, Cu-MOF, and NiAl-LDH [63].

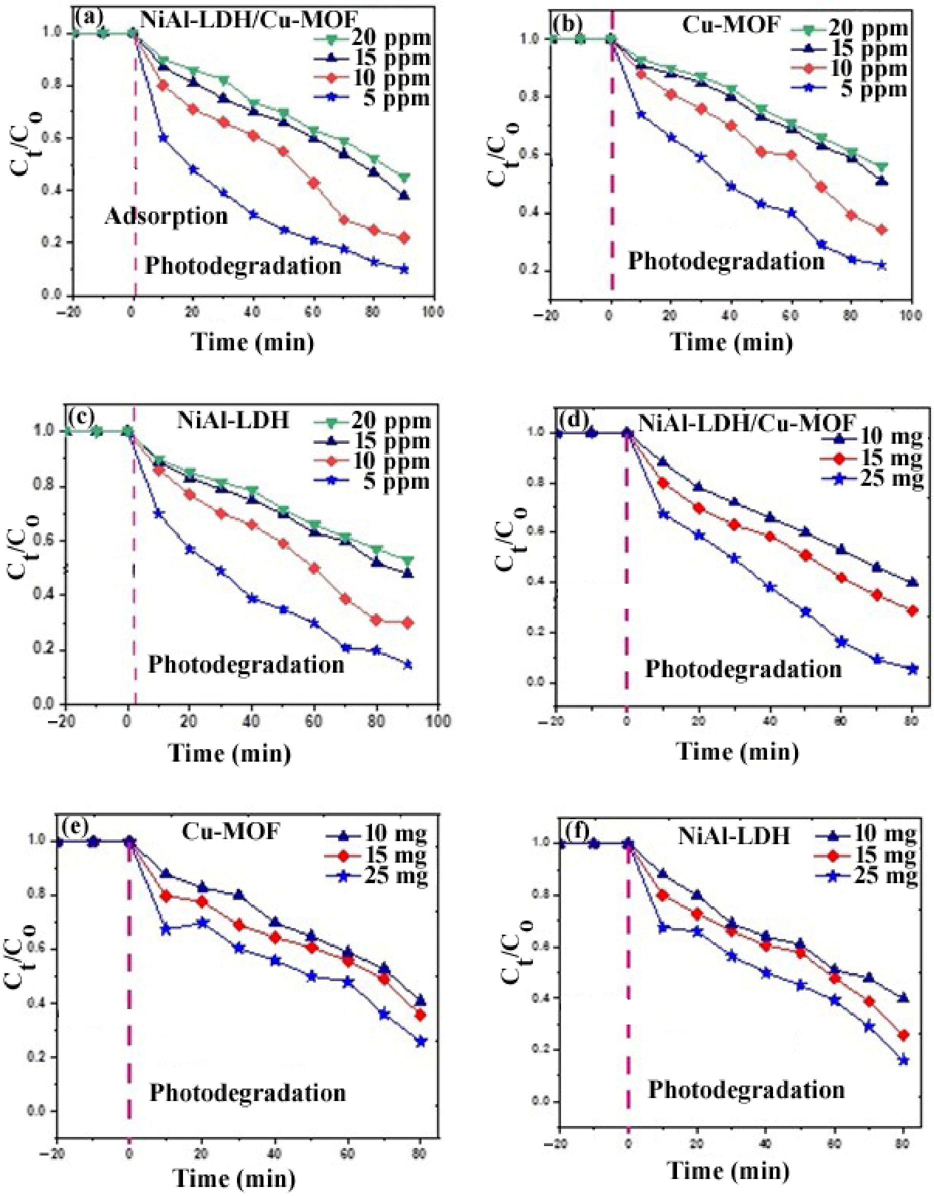

Figure 8. (**a**–**c**) Photocatalytic degradation of MO at varied dye concentrations (5, 10, and 15 ppm) by NiAl-LDH/Cu-MOF composite, Cu-MOF, and NiAl-LDH and (**d**–**f**) and at varied photocatalyst concentrations (10, 15, and 25 ppm) by NiAl-LDH/Cu-MOF composite, Cu-MOF, and NiAl-LDH.

2.10.4. Effect of Photocatalyst Amount

The degradation efficiency was studied by increasing the catalyst dose of 10, 15, and 25 mg in a 30 mL solution of 5×10^{-5} M MO dye. The results are shown in Figure 8d–f. In dark or before sunlight irradiation, no changes were found in the MO dye solution after the addition of different concentrations of the NiAl-LDH/Cu-MOF composite, Cu-MOF, and NiAl-LDH and the color of the dye does not change, which means that adsorption efficiency is very low or almost zero [56]. However, after irradiation with sunlight, the NiAl-LDH/Cu-MOF composite exhibits maximum degradation efficiency compared to Cu-MOF and NiAl-LDH at a 25 mg concentration. As the amount of photocatalyst enhances, the degradation ability also increases due to the more significant number of active sites. This leads to more dye molecules trapped on the photocatalyst surface, resulting in more considerable degradation. The improved degradation efficiency can be attributed to the larger surface area available, which increases the number of active sites on the catalyst's surface as the photocatalyst dosage increases [64]. Existing literature on the topic indicates that an increase in the photocatalyst dose of LDHs may result in the aggregation of the LDH sheets, reducing the material's surface area and obscuring active sites [65]. Exceeding the optimal concentration of photocatalysts results in the complete saturation of active sites. Consequently, light is scattered rather than penetrating, which leads to decreased efficacy and eventual deterioration [66].

2.10.5. Hydrogen Peroxide (H_2O_2) Concentration Effect

The study focused on investigating how the amount of H_2O_2 variation in the range of 15–20 mmol affected the degradation of dyes, while keeping other factors such as pH, time, dye, and catalyst concentration constant, as shown in Figure 9a. In the dark or before sunlight irradiation, no changes were found in the MO dye solution after the addition of different concentrations of H_2O_2 with the NiAl-LDH/Cu-MOF composite and the color of the dye does not change, which means that adsorption efficiency is very low or almost zero [56]. However, after irradiation to sunlight, maximum degradation efficiency was exhibited by the NiAl-LDH/Cu-MOF composite at a 20 mmol H_2O_2 concentration. It was discovered that increasing the dosage of H_2O_2 resulted in an intensified deterioration of dyes because H_2O_2 acts as an oxidizing agent, producing hydroxide radicals (OH^-) and preventing the recombination of electron–hole pairs [67].

$$H_2O_2 + O_2^{-\cdot} \rightarrow OH^{\cdot} + O_2 + OH^- \tag{11}$$

$$H_2O_2 + e_{CB}^- \rightarrow OH^{\cdot} + OH^{-\cdot} \tag{12}$$

$$H_2O_2 + hv \rightarrow 2OH^{\cdot} \tag{13}$$

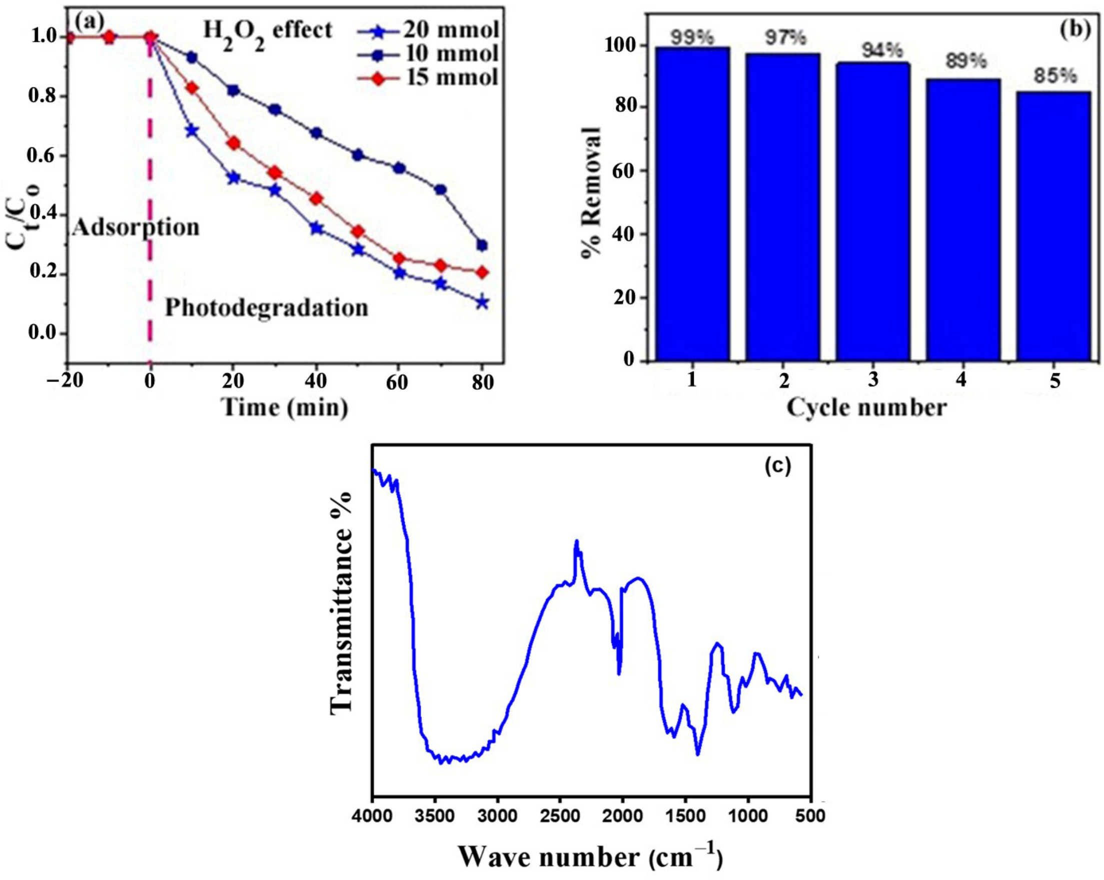

Figure 9. (**a**) Effect of concentration of H_2O_2 on the degradation of MO dye by photocatalyst NiAl-LDH/Cu-MOF, (**b**) Recyclability of NiAl-LDH/Cu-MOF composite for MO dye degradation and (**c**) FTIR spectrum of NiAl-LDH/Cu-MOF composite after five cycles.

2.10.6. Recyclability of the Photocatalyst

The effectiveness of photocatalysts in dye degradation is closely tied to their stability and reusability. A high-quality photocatalyst should maintain its catalytic activity over extended periods and multiple cycles of use [68]. This is because the process of dye degradation often involves complex reactions that can degrade the photocatalyst or reduce its activity if not properly managed. Photocatalysts that lose efficiency quickly are less practical, even if they exhibit high initial performance. Reusability indicates a photocatalyst's robustness and stability [69]. A catalyst that can withstand repeated use without significant performance loss demonstrates its reliability and effectiveness. This means that the degradation process remains efficient, ensuring consistent removal of dyes and other pollutants [70].

The capacity of MO to be degraded by NiAl-LDH/Cu-MOF was tested over five regeneration cycles (Figure 9b). After the first run, the degradation efficiencies were 99%, 97%, 94%, 89%, and 85%, showing the stable nature of NiAl-LDH/Cu-MOF composite. The FTIR spectrum (Figure 9c) after five cycles validates the stability of composite. Additionally, the regeneration of NiAl-LDH/Cu-MOF is reported to be possible with only a slight and progressive decline in degradation efficacy, indicating an essential eco-efficient characteristic [71]. The gradual decrease in surface crystallinity during the composite regeneration and adding a small amount of pollutant degradation products to the regenerated materials can account for the decline in degradation values [72]. After the fifth cycle, the catalyst's stability decreased, possibly due to the upper layer of the catalyst being poisoned by adsorbed intermediate substances. These intermediates can take up the active sites on the catalyst's surface, leading to a decline in the catalyst's photocatalytic activity [73]. After the fifth cycle, the decrease in removal efficiency may also be due to photo-corrosion occurrence due to long-term light irradiation [73].

Photodegradation Kinetics

Two models (pseudo-first–order and Langmuir–Hinshelwood (L–H)) were used to deteriorate MO dye under sunlight using NiAl-LDH/Cu-MOF, as shown in Figure 10. The equation for the first-order model can be shown as follows:

$$\ln\left(\frac{C_t}{C_0}\right) = -kt \tag{14}$$

where C_t and C_0 are initial and final concentrations. The pseudo-first-order reaction degradation rate constant is k. The pseudo-first-order degradation rate constant was determined by plotting $\ln(C_t/C_0)$ versus time, using MO dye concentrations of 5, 10, 15, and 20 ppm. The following equation can express the L–H model:

$$\frac{1}{K_{obs}} = \frac{1}{K_C K_{L-H}} + C_0/K_C \tag{15}$$

where K is the rate coefficient for first-order degradation; K_C represents the superficial reaction rate constant in $\text{mgL}^{-1}\ \text{min}^{-1}$, and C_0 and $K_{L\text{-}H}$ are the initial dye concentration and the adsorption constant in mg/L and L/mg, respectively. The L–H model was plotted as a relationship between $1/K_{obs}$ and C_0 [56].

L–H and pseudo-first-order reactions were observed for the photodeterioration where K is the rate coefficient for the first-order degradation of MO dye, and the analyzed data are presented in Table 1 and Figure 10. The data analysis indicates that the experimental results align with the L–H and pseudo-first-order models.

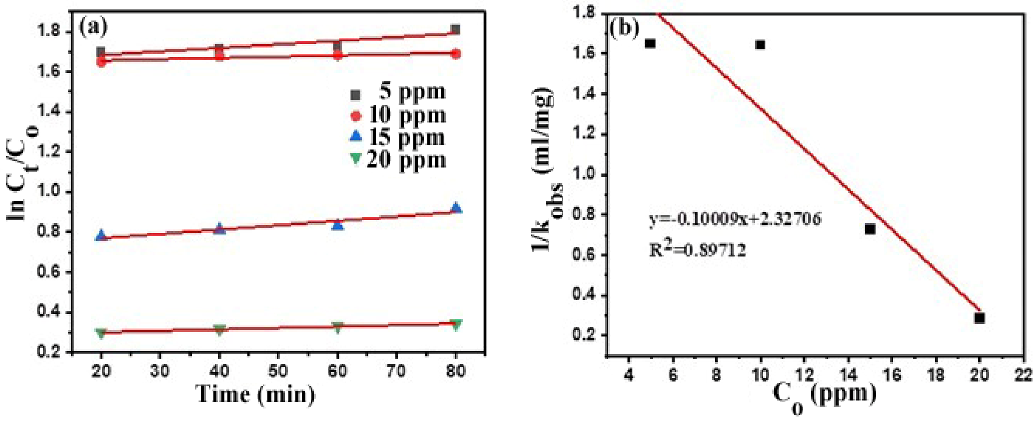

Figure 10. (**a**) Modeling the pseudo first order for the photodegradation of MO dye using NiAl-LDH/Cu-MOF and (**b**) variation in the rate constant of reaction with different initial dosages of MO dye.

Table 1. The data of kinetics for photocatalytic removal of MO dye by NiAl-LDH/Cu-MOF [56].

Initial Concentration (ppm)	R^2	$1/k_{obs}$	Equation of a Straight Line
5	0.79	1.648	$y = -1.0 \times 10^{-3} x + 1.648$
10	0.73	1.643	$y = 6.5 \times 10^{-4} x + 1.643$
15	0.86	0.726	$y = 2.0 \times 10^{-3} x + 0.726$
20	0.99	0.285	$y = 7.2 \times 10^{-4} x + 0.285$

Antibacterial Activity

Incorporating antibacterial activity into the NiAl-LDH/Cu-MOF catalyst used for dye degradation addresses the chemical removal of pollutants and the prevention of bacterial issues. This dual functionality improves the treatment process's effectiveness, safety, and practicality.

The antibacterial activities of NiAl-LDH/Cu-MOF, Cu-MOF, and NiAl-LDH against Gram positive (*Staphylococcus aureus, Enterococcus faecalis*) and Gram negative (*Escherichia coli*, *Pseudomonas fluorescens*) bacteria with MIC and MIB concentrations were studied using the disk diffusion method, as depicted in Figure 11 and supporting information (Table S1).

From the results, it can be inferred that NiAl-LDH/Cu-MOF achieved the maximum MIC concentration with Gram negative bacteria (*E. coli*) rather than Gram-positive bacteria, as shown in Table S2. The thickness of the cell walls of bacteria can explain the interaction between bacteria and NiAl-LDH/Cu-MOF. The thickness range for Gram-negative and Gram-positive bacteria is 5–10 nm and 20–80 nm, respectively. Gram-positive bacteria have thick single-cell walls with peptidoglycan layers. In contrast, Gram-negative bacteria have double-thin lipopolysaccharide and peptidoglycan layers. The NiAl-LDH/Cu-MOF composite can change the structure of cell walls by enhancing diffusion into the intracellular space, ultimately resulting in cell death. The findings indicate that Gram-negative bacteria are more vulnerable to the NiAl-LDH/Cu-MOF composite due to their positive charge, enabling a more effective interaction with cell membranes than Gram-positive bacteria. Comparable results can be found in the existing literature [74–76].

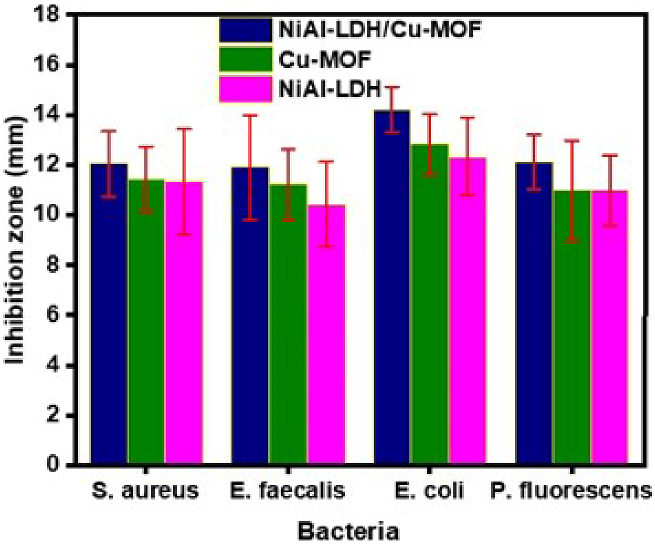

Figure 11. Antibacterial activity of NiAl-LDH/Cu-MOF composite, Cu-MOF, and NiAl-LDH catalyst.

3. Experimental Section

3.1. Materials and Synthesis Methods

Nickel nitrate hexahydrate ($Ni(NO_3)_2 \cdot 6H_2O$) and aluminum nitrate nonahydrate ($Al(NO_3)_3 \cdot 9H_2O$) with 99% purity were purchased from Sigma-Aldrich (Saint Louis, MO, USA); sodium hydroxide pellets (NaOH), copper acetate hydrate ($Cu(OAc)_2 \cdot xH_2O$), and terephthalic acid ($C_6H_4(CO_2H)_2$) with 98% purity were purchased from Sigma-Aldrich; N-hexane, N,N-dimethylformamide, and copper nitrate trihydrate ($Cu(NO_3)_2 \cdot 3H_2O$) with 99% purity were purchased from Sigma-Aldrich. Methyl orange dye ($C_{14}H_{14}N_3Na0_3S$) with 85% purity was purchased from Sigma Aldrich.

3.2. Preparation of NiAl-LDH

The co-precipitation approach was chosen to synthesize NiAl-LDH [77]. Nitrate salts of nickel and aluminum were mixed in a 3:1 molar ratio with deionized (DD) water and continuously agitated to form a homogeneous mixture. Gradually, 2 N NaOH solution was added to the above mixture with steady stirring at 60 °C to maintain the pH of the solution at 10. The blend was placed on a hot plate with continuous stirring for 15 h. The greenish-colored precipitate was collected by centrifugation after the complete reaction. The newly synthesized photocatalyst underwent multiple rounds of rinsing with deionized water to eliminate contaminants until the pH of the solution attained a stable level. Finally, the NiAl-LDH was dried at 80 °C for 10 h and then converted into powder using a mortar and pestle.

3.3. Synthesis of Cu-MOF

Two mmol $Cu(OAc)_2 \cdot xH_2O$ and 1 mmol of terephthalic acid were added in 10 mL of water and 10 mL of N-hexane, respectively. A few drops of triethylamine were added to the terephthalic acid solution to increase solubility. The two prepared solutions were thoroughly mixed and refluxed for 2 h. The resulting precipitates were centrifuged for 5 min at approximately 6000 rpm. The precipitates (Cu-MOF) were washed with ethanol and repeatedly rinsed with water before drying in an oven at about 70 °C.

3.4. Synthesis of NiAl-LDH/Cu-MOF Composite

NiAl-LDH/Cu-MOF composite was synthesized using a simple thermal impregnation strategy. First, 20 mmol of Cu-MOF was mixed with a certain quantity of distilled water and sonicated for 20 min. The previously synthesized NiAl-LDH was then added to the suspension, which was sonicated for 20 min and then heated at 70 °C for 2 h. The solution was then cooled, filtered, and rinsed with alcohol to remove residual materials. The resulting greenish-blue product was dried and pulverized to obtain a fine powder designated as NiAl-LDH/Cu-MOF composite.

3.5. Photocatalytic Degradation Experiment

The reaction was initiated to evaluate the influence of dye amounts, pH, catalyst conc., and reaction time on the percentage degradation of MO dye using three prepared photocatalysts: NiAl-LDH, Cu-MOF, and NiAl-LDH/Cu-MOF composite. For this study, 30 mL of a 5 ppm MO dye solution in water was mixed with 25 mg of photocatalyst, stirred at room temperature for about 30 min to achieve adsorption/desorption equilibrium, and then exposed to sunlight. Absorbance was noted at 460 nm using a UV–visible spectrometer before and after sunlight irradiation. The removal efficiency was calculated using the provided formulas [78,79].

$$R = \frac{C_o - C_e}{C_n} \times 100 \tag{16}$$

C_0 and C_e represent the initial and equilibrium concentrations of MO dye in mg/L, respectively.

To investigate the effect of pH, solutions with pH ranges of 2 to 12 were prepared using 1 N NaOH and HCl, with the amount of photocatalyst kept constant at 25 mg in each case. To study the time effect on MO deterioration, 30 mL of dye solution with 25 mg of photocatalyst was used and absorbance was monitored over time, showing a continuous degradation curve from maximum to minimum absorbance intensity. For evaluating the effect of dye concentration, solutions with dye concentrations of 5, 10, 15, and 20 ppm were used while keeping the amount of photocatalyst constant. The amounts of photocatalyst were 10, 15, and 25 mg while using a 5×10^{-5} M dye solution. The impact of H_2O_2 concentration was conducted within the 15–20 mmol range. All these parameters were studied before and after sunlight exposure.

3.6. Reusability of the Photocatalyst

The reusability of photocatalysts is paramount from an environmental perspective. Photocatalysts are substances that facilitate the degradation of pollutants by generating reactive species under light irradiation [80]. Traditional dye removal methods often involve using large quantities of chemicals or physical adsorbents that are either not recyclable or used only once [81]. In contrast, a reusable photocatalyst can repeatedly perform its function, significantly reducing the need for new materials and minimizing waste generation. This aligns with the principles of sustainable development, which advocate for the efficient use of resources and the reduction of environmental impact [82,83].

To assess the regeneration of the NiAl-LDH/Cu-MOF composite, a series of degradation processes were conducted on the prepared sample under sunlight and an MO dosage of 25 mg/L. This process was performed five times, and the degradation efficiency for each cycle was determined.

3.6.1. Antibacterial Study

In water treatment systems, bacterial growth on the surface of catalysts (biofouling) can reduce their effectiveness. Antibacterial properties help prevent or minimize biofouling, ensuring the catalytic activity remains high over time. By controlling bacterial contamination, the performance and longevity of the catalyst are preserved, leading to more reliable and sustained degradation of pollutants [84,85].

The methodologies utilized in the bioassays were meticulously crafted, adhering to the esteemed standards of the Clinical and Laboratory Standards Institute (CLSI). These standards, widely recognized and utilized by disk diffusion methods (M7-A7) and for Antibacterial Agents Sensitivity Tests M2-A8 for Sanitary Surveillance from the National Agency (Anvisa), were followed in this research for compound solubilization by using organic solvents.

3.6.2. Minimal Inhibitory Concentration (MIC)

MIC was examined with utmost precision by applying the broth macro-dilution method. Compound dilutions of 2:1 (1000, 500, 250, 125, and 62.5) were meticulously assessed in the solvent possessing the best solubility, with intermediary values (200, 400, 300, and 600) obtained. The produced inoculum was prepared by utilizing bacterial colonies with incubation times < 24 h, then adjusted to 0.5 of bacterial turbidity of the McFarland standard solution in a dosage of 1.5×10^8 CFUs/mL. Here, CFUs/mL is colony-forming units for mL and, following, the dosage of 5×10^5 CFUs/mL with Luria–Bertani broth. One mL of the bacterial suspension and test solution with a specific dosage was put into test tubes to examine the MIC, except in the negative control tube. Bacterial growth and turbidity were assessed by incubating at 35 ± 2 °C for almost 20 h. The MIC, capable of inhibiting bacterial growth, was calculated as the lowest dosage value of the compound. Positive and negative control tubes with adjusted bacterial growth and LB broth and low LB broth dosage without inoculum, respectively, were separated. The bioassays with three repetitions were conducted twice for each bacterial strain; upon detecting any error or presence of contamination, the result was neglected and the test was performed again.

3.6.3. Minimum Bactericidal Concentration (MBC)

MBC was assessed rigorously using the Petri dish sowing method, like the MIC calculation procedure. After incubation, 0.1 mL of aliquot was taken from each test tube to calculate the MIC. The inoculum was spread on the culture medium's outer layer in Petri plates using a Drigalski spatula. The Petri dishes were then incubated for 20 h at 35 ± 2 °C, and bacterial colonies in each plate were analyzed. The MBC is defined as the lowest dosage of the compound capable of preventing the growth of microbes in the culture medium. Each strain of bacteria was subjected to bioassays twice with three repetitions. If an error or contamination was detected, the result was disregarded and the analysis was repeated.

3.6.4. Disk Diffusion Method for Testing Antibacterial Sensibility

The antibacterial test, also called an antibiogram, was performed using the Kirby–Bauer method or disk diffusion. Sterile filter paper discs saturated with the minimum inhibitory concentration (MIC) solution were utilized for each compound. The culture medium was placed on 90 mm diameter Petri dishes and then incubated before preparing a bacterial inoculum using a standard 0.5 McFarland scale solution. The inoculum was spread evenly on the culture medium using a sterile swab, and the plates were then incubated for 18 h at 35 ± 2 °C. The inhibition zones were measured and statistically analyzed using Tukey's test ($p < 0.05$), ANOVA, and the Kruskal–Wallis test ($p < 0.05$).

4. Conclusions

Numerous steps are being taken to mitigate the effects of water contamination, a primary global concern. Water is often polluted with various substances, including heavy metals and dyes. The NiAl-LDH/Cu-MOF composite was synthesized from pre-synthesized NiAl-LDH and Cu-MOF through thermal impregnation to remove MO dye from contaminated water. The resulting NiAl-LDH/Cu-MOF was thoroughly characterized using FTIR, XRD, SEM, DRS, and TGA techniques. The FTIR spectrum of NiAl-LDH/Cu-MOF/dye confirmed that the dye molecule was degraded by NiAl-LDH/Cu-MOF. The designed NiAl-LDH/Cu-MOF exhibited excellent degradation capability, achieving 99% dye removal. NiAl-LDH alone exhibited a 94% removal efficiency, while Cu-MOF showed an 82% removal rate. The degradation kinetics followed a pseudo-first-order and Langmuir–Hinshelwood model with $R^2 = 0.94$. After five regeneration cycles, the removal efficiency of NiAl-LDH/Cu-MOF for MO decreased to 86.7%. Antibacterial activity was also performed with antibacterial sensibility testing by disk diffusion to determine minimal inhibitory and bactericidal concentrations. The NiAl-layered double hydroxide/copper metal–organic framework photocatalyst offers enhanced photocatalytic activity, efficient ROS generation, increased surface area, and stability, all of which contribute to its antibacterial potential and effectiveness in degrading methyl orange dye. Its dual functionality enhances dye degradation efficiency and addresses bacterial contamination, making it a valuable tool for environmental remediation and public health applications.

Supplementary Materials: The following supporting information can be downloaded at https://www.mdpi.com/article/10.3390/catal14100719/s1, Table S1: Results of the minimal inhibitory concentration (MIC) and the minimal bactericidal concentration (MBC) for the compounds evaluated, expressed in µg/mL; Table S2: Diameter of the inhibition zone, average, and standard deviation (mm), by NiAl-LDH/Cu-MOF, Cu-MOF, and NiAl-LDH.

Author Contributions: Methodology, I.B., S.A., F.A. and M.B.T.; formal analysis, D.F.B., A.A., F.M.H.A. and O.M.A.; data curation, S.A., R.H.A., A.N., M.K.N. and I.M.; writing—original draft, I.B. and M.B.T.; writing—review and editing, M.B.T., O.M.A., S.A.C.C., M.I.K. and J.F.-G.; visualization, A.S. and J.F.-G.; supervision, S.A.C.C. and M.B.T.; project administration, M.B.T., O.M.A., J.F.-G. and M.I.K. All authors have read and agreed to the published version of the manuscript.

Funding: This research was funded by Taif University, Saudi Arabia, project number (TU-DSPP-2024-276).

Data Availability Statement: All data are presented within the manuscript body.

Acknowledgments: The authors extend their appreciation to the Higher Education Commission, Pakistan and Fundação para a Ciência e Tecnologia and Ministério da Ciência, Tecnologia e Ensino Superior (project DOIs: 10.54499/LA/P/0008/2020, 10.54499/UIDP/50006/2020, and 10.54499/UIDB/50006/2020 and Scientific Employment Stimulus—Institutional Call DOI 10.54499/CEECINST/00102/2018/CP1567/CT0026). IQS-School of Engineering and GESPA group are recognized as a Consolidated Research Group by the Catalan Government (2021 SGR 00321). They also acknowledge funding from the project HEC-A20.1267.

Conflicts of Interest: The authors declare no conflicts of interest.

References

1. Alvi, M.; Al-Ghamdi, A.; ShaheerAkhtar, M. Synthesis of ZnO nanostructures via low temperature solution process for photocatalytic degradation of rhodamine B dye. *Mater. Lett.* **2017**, *204*, 12–15. [CrossRef]
2. Li, S.; Cai, M.; Liu, Y.; Wang, C.; Yan, R.; Chen, X. Constructing $Cd_{0.5}Zn_{0.5}S/Bi_2WO_6$ S-scheme heterojunction for boosted photocatalytic antibiotic oxidation and Cr (VI) reduction. *Adv. Powder Mater.* **2023**, *2*, 100073. [CrossRef]
3. Gürses, A.; Açıkyıldız, M.; Güneş, K.; Gürses, M.S. Classification of dye and pigments. In *Dyes and Pigments*; Springer: Berlin/Heidelberg, Germany, 2016; pp. 31–45.
4. Jana, S.; Konar, S.; Mitra, B.C.; Mondal, A.; Mukhopadhyay, S. Fabrication of a new heterostructure $Au/Pt/SnO_2$: An excellent catalyst for fast reduction of para-nitrophenol and visible light assisted photodegradation of dyes. *Mater. Res. Bull.* **2021**, *141*, 111351. [CrossRef]
5. Alghamdi, Y.G.; Krishnakumar, B.; Malik, M.A.; Alhayyani, S. Design and preparation of biomass-derived activated carbon loaded TiO_2 photocatalyst for photocatalytic degradation of reactive red 120 and ofloxacin. *Polymers* **2022**, *14*, 880. [CrossRef]
6. Darvishi Cheshmeh Soltani, R.; Rezaee, A.; Safari, M.; Khataee, A.; Karimi, B. Photocatalytic degradation of formaldehyde in aqueous solution using ZnO nanoparticles immobilized on glass plates. *Desalin. Water Treat.* **2015**, *53*, 1613–1620. [CrossRef]
7. Alsulaim, G.M. New $BaTi_{0.96}Cu_{0.02}X_{0.02}O_3$ (X = V, Nb) Photocatalysts for Dyes Effluent Remediation: Broad Visible Light Response. *Catalysts* **2023**, *13*, 1365. [CrossRef]
8. Pahalagedara, M.N.; Samaraweera, M.; Dharmarathna, S.; Kuo, C.-H.; Pahalagedara, L.R.; Gascón, J.A.; Suib, S.L. Removal of azo dyes: Intercalation into sonochemically synthesized NiAl layered double hydroxide. *J. Phys. Chem. C* **2014**, *118*, 17801–17809. [CrossRef]
9. Islam, D.; Borah, D.; Acharya, H. Controlled synthesis of monodisperse silver nanoparticles supported layered double hydroxide catalyst. *RSC Adv.* **2015**, *5*, 13239–13245. [CrossRef]
10. Cheng, Z.-L.; Liu, Y.-Y.; Cao, B.-C. Two-dimensional layered structure-templated synthesis of graphene nanosheets using CoAl-LDH under low carbonization temperature. *Mater. Lett.* **2016**, *175*, 215–218. [CrossRef]
11. Gao, Z.; Liang, J.; Yao, J.; Meng, Q.; He, G.; Chen, H. Synthesis of Ce-doped NiAl LDH/RGO composite as an efficient photocatalyst for photocatalytic degradation of ciprofloxacin. *J. Environ. Chem. Eng.* **2021**, *9*, 105405. [CrossRef]
12. Haque, E.; Lee, J.E.; Jang, I.T.; Hwang, Y.K.; Chang, J.-S.; Jegal, J.; Jhung, S.H. Adsorptive removal of methyl orange from aqueous solution with metal-organic frameworks, porous chromium-benzenedicarboxylates. *J. Hazard. Mater.* **2010**, *181*, 535–542. [CrossRef]

13. Furukawa, H.; Cordova, K.E.; O'Keeffe, M.; Yaghi, O.M. The chemistry and applications of metal-organic frameworks. *Science* **2013**, *341*, 1230444. [CrossRef]
14. Li, S.; Dong, K.; Cai, M.; Li, X.; Chen, X. A plasmonic S-scheme Au/MIL-101 (Fe)/BiOBr photocatalyst for efficient synchronous decontamination of Cr (VI) and norfloxacin antibiotic. *EScience* **2024**, *4*, 100208. [CrossRef]
15. Salama, R.S.; El-Hakam, S.; Samra, S.; El-Dafrawy, S.; Ahmed, A. Adsorption, equilibrium and kinetic studies on the removal of methyl orange dye from aqueous solution by using of copper metal organic framework (Cu-BDC). *Int. J. Mod. Chem* **2018**, *10*, 195–207.
16. Elizalde-Velázquez, A.; Gómez-Oliván, L.M.; Galar-Martínez, M.; Islas-Flores, H.; Dublán-García, O.; SanJuan-Reyes, N. Amoxicillin in the aquatic environment, its fate and environmental risk. *InTech* **2016**, *1*, 247–267.
17. Bhuyan, A.; Ahmaruzzaman, M. Ultrasonic-assisted synthesis of highly efficient and robust metal oxide QDs immobilized-MOF-5/Ni-Co-LDH photocatalyst for sunlight-mediated degradation of multiple toxic dyes. *J. Alloys Compd.* **2024**, *972*, 172781. [CrossRef]
18. Li, Y.; Zhang, A.; Liu, Z.; Yao, S.; Zhou, R.; Fu, Y.; Zhou, Q. A study on the role of high-energy holes and reactive oxygen species in photocatalytic degradation using oxygen-doped/biochar-modified 2D carbon nitride. *J. Water Process Eng.* **2024**, *65*, 105808. [CrossRef]
19. Mohamadpour, F.; Amani, A.M. Photocatalytic systems: Reactions, mechanism, and applications. *RSC Adv.* **2024**, *14*, 20609–20645. [CrossRef]
20. Ubaldi, F.; Valeriani, F.; Volpini, V.; Lofrano, G.; Romano Spica, V. Antimicrobial Activity of Photocatalytic Coatings on Surfaces: A Systematic Review and Meta-Analysis. *Coatings* **2024**, *14*, 92. [CrossRef]
21. Du, T.; Zhang, H.; Ruan, J.; Jiang, H.; Chen, H.-Y.; Wang, X. Adjusting the linear range of Au-MOF fluorescent probes for real-time analyzing intracellular GSH in living cells. *ACS Appl. Mater. Interfaces* **2018**, *10*, 12417–12423. [CrossRef]
22. Carson, C.G.; Hardcastle, K.; Schwartz, J.; Liu, X.; Hoffmann, C.; Gerhardt, R.A.; Tannenbaum, R. Synthesis and structure characterization of copper terephthalate metal–organic frameworks. *Eur. J. Inorg. Chem.* **2009**, *2009*, 2338–2343. [CrossRef]
23. Wang, R.; Li, Q.; Duan, N.; Zhang, T.; Lu, H. Preparation of biomorphic Ni–Al LDHs using cotton from discarded T–shirt as a template and the adsorption capability for Congo red. *Res. Chem. Intermed.* **2015**, *41*, 7899–7914. [CrossRef]
24. Lesbani, A.; Normah, N.; Palapa, N.R.; Taher, T.; Andreas, R.; Mohadi, R. Ni/Al Layered Double Hydroxide Intercalated with Keggin Ion [α-SiW12O40]4-for Iron (II) Removal in Aqueous Solution (Similarity). *Molekul* **2020**, *15*, 149–157. [CrossRef]
25. Li, L.; San Hui, K.; Hui, K.N.; Xia, Q.; Fu, J.; Cho, Y.-R. Facile synthesis of NiAl layered double hydroxide nanoplates for high-performance asymmetric supercapacitor. *J. Alloys Compd.* **2017**, *721*, 803–812. [CrossRef]
26. Zheng, W.; Sun, S.; Xu, Y.; Yu, R.; Li, H. Sulfidation of hierarchical NiAl−LDH/Ni−MOF composite for high-performance supercapacitor. *ChemElectroChem* **2019**, *6*, 3375–3382. [CrossRef]
27. Yan, X.; Jin, Z. Interface engineering: NiAl-LDH in-situ derived NiP_2 quantum dots and Cu_3P nanoparticles ingeniously constructed pn heterojunction for photocatalytic hydrogen evolution. *Chem. Eng. J.* **2021**, *420*, 127682. [CrossRef]
28. Verónica, M.; Graciela, B.; Norma, A.; Miguel, L. Ethanol steam reforming using Ni(II)-Al(III) layered double hydroxide as catalyst precursor: Kinetic study. *Chem. Eng. J.* **2008**, *138*, 602–607. [CrossRef]
29. Perez-Bernal, M.E.; Ruano-Casero, R.J.; Benito, F.; Rives, V. Nickel–aluminum layered double hydroxides prepared via inverse micelles formation. *J. Solid State Chem.* **2009**, *182*, 1593–1601. [CrossRef]
30. Mas, V.; Dieuzeide, M.L.; Jobbágy, M.; Baronetti, G.; Amadeo, N.; Laborde, M. Ni(II)-Al(III) layered double hydroxide as catalyst precursor for ethanol steam reforming: Activation treatments and kinetic studies. *Catal. Today* **2008**, *133*, 319–323. [CrossRef]
31. Yang, J.-F.; Zhou, Z.-T. Use of spray technique to prepare Ni/Al-layered double hydroxides. *J. Alloys Compd.* **2009**, *473*, 458–461. [CrossRef]
32. Wang, H.; Zheng, C.; Li, F. Biopolymer-induced microstructure-controlled fabrication of Ni–Al layered double hydroxide films. *Chem. Eng. J.* **2010**, *158*, 633–640. [CrossRef]
33. Popova, L.; Pancheva, T.; Uzunova, A. Salicylic acid: Properties, biosynthesis and physiological role. *Bulg. J. Plant Physiol* **1997**, *23*, 85–93.
34. Abdolmohammad-Zadeh, H.; Kohansal, S.; Sadeghi, G. Nickel–aluminum layered double hydroxide as a nanosorbent for selective solid-phase extraction and spectrofluorometric determination of salicylic acid in pharmaceutical and biological samples. *Talanta* **2011**, *84*, 368–373. [CrossRef]
35. Rodenas, T.; Luz, I.; Prieto, G.; Seoane, B.; Miro, H.; Corma, A.; Kapteijn, F.; Llabrés i Xamena, F.X.; Gascon, J. Metal–organic framework nanosheets in polymer composite materials for gas separation. *Nat. Mater.* **2015**, *14*, 48–55. [CrossRef]
36. Zhan, G.; Fan, L.; Zhao, F.; Huang, Z.; Chen, B.; Yang, X.; Zhou, S.F. Fabrication of ultrathin 2D Cu-BDC nanosheets and the derived integrated MOF nanocomposites. *Adv. Funct. Mater.* **2019**, *29*, 1806720. [CrossRef]
37. Liu, P.-F.; Tao, K.; Li, G.-C.; Wu, M.-K.; Zhu, S.-R.; Yi, F.-Y.; Zhao, W.-N.; Han, L. In situ growth of ZIF-8 nanocrystals on layered double hydroxide nanosheets for enhanced CO_2 capture. *Dalton Trans.* **2016**, *45*, 12632–12635. [CrossRef]
38. Liu, Y.; Wang, N.; Pan, J.H.; Steinbach, F.; Caro, J.R. In situ synthesis of MOF membranes on ZnAl-CO_3 LDH buffer layer-modified substrates. *J. Am. Chem. Soc.* **2014**, *136*, 14353–14356. [CrossRef]
39. Rani, R.; Deep, A.; Mizaikoff, B.; Singh, S.J.V. Enhanced hydrothermal stability of Cu MOF by post synthetic modification with amino acids. *Vacuum* **2019**, *164*, 449–457. [CrossRef]

40. Abdelmoaty, A.S.; El-Beih, A.A.; Hanna, A.A. Synthesis, characterization and antimicrobial activity of copper-metal organic framework (Cu-MOF) and its modification by melamine. *J. Inorg. Organomet. Polym. Mater.* **2022**, *32*, 1778–1785. [CrossRef]
41. dos Santos, R.M.M.; Gonçalves, R.G.L.; Constantino, V.R.L.; Santilli, C.V.; Borges, P.D.; Tronto, J.; Pinto, F.G. Adsorption of Acid Yellow 42 dye on calcined layered double hydroxide: Effect of time, concentration, pH and temperature. *Appl. Clay Sci.* **2017**, *140*, 132–139. [CrossRef]
42. Constantino, V.R.; Pinnavaia, T.J. Basic properties of Mg2+ 1-xAl3+ x layered double hydroxides intercalated by carbonate, hydroxide, chloride, and sulfate anions. *Inorg. Chem.* **1995**, *34*, 883–892. [CrossRef]
43. Guo, H.; Wang, Y.; Li, C.; Zhou, K. Construction of sandwich-structured CoAl-layered double hydroxide@zeolitic imidazolate framework-67 (CoAl-LDH@ZIF-67) hybrids: Towards enhancing the fire safety of epoxy resins. *RSC Adv.* **2018**, *8*, 36114–36122. [CrossRef]
44. Taghavi Fardood, S.; Moradnia, F.; Heidarzadeh, S.; Naghipour, A. Green synthesis, characterization, photocatalytic and antibacterial activities of copper oxide nanoparticles of copper oxide nanoparticles. *Nanochem. Res.* **2023**, *8*, 134–140.
45. Jubu, P.R.; Obaseki, O.; Ajayi, D.; Danladi, E.; Chahrour, K.M.; Muhammad, A.; Landi, S., Jr.; Igbawua, T.; Chahul, H.; Yam, F. Considerations about the determination of optical bandgap from diffuse reflectance spectroscopy using the Tauc plot. *J. Opt.* **2024**, 1–11. [CrossRef]
46. Jubu, P.R.; Danladi, E.; Ndeze, U.; Adedokun, O.; Landi, S., Jr.; Haider, A.; Adepoju, A.; Yusof, Y.; Obaseki, O.; Yam, F. Comment about the use of unconventional Tauc plots for bandgap energy determination of semiconductors using UV–Vis spectroscopy. *Results Opt.* **2024**, *14*, 100606. [CrossRef]
47. Rajput, A.; Rahman, M.A.; Rahman, M.H.; Kuila, A. Visible light photocatalytic degradation of organic pollutants in industrial wastewater by engineered TiO_2 nanoparticles. *Biomass Convers. Biorefinery* **2024**, *14*, 17301–17311. [CrossRef]
48. Kong, C.; Min, S.; Lu, G. Dye-sensitized NiSx catalyst decorated on graphene for highly efficient reduction of water to hydrogen under visible light irradiation. *ACS Catal.* **2014**, *4*, 2763–2769. [CrossRef]
49. Maseeh, I.; Anwar, F.; Aroob, S.; Javed, T.; Bibi, I.; Almasoudi, A.; Raheel, A.; Javid, M.A.; Carabineiro, S.A.; Taj, M.B. Multifunctional MgAl LDH/Zn-MOF S-scheme heterojunction: Efficient hydrogen production, methyl red removal, and CO_2 adsorption. *Mater. Adv.* **2024**, *5*, 5080–5095. [CrossRef]
50. Li, X.; Yu, J.; Low, J.; Fang, Y.; Xiao, J.; Chen, X. Engineering heterogeneous semiconductors for solar water splitting. *J. Mater. Chem. A* **2015**, *3*, 2485–2534. [CrossRef]
51. Derikvandi, H.; Vosough, M.; Nezamzadeh-Ejhieh, A. A novel double Ag@AgCl/Cu@Cu_2O plasmonic nanostructure: Experimental design and LC-Mass detection of tetracycline degradation intermediates. *Int. J. Hydrogen Energy* **2021**, *46*, 2049–2064. [CrossRef]
52. Mahmoodi, N.M.; Arami, M.; Limaee, N.Y.; Tabrizi, N.S. Kinetics of heterogeneous photocatalytic degradation of reactive dyes in an immobilized TiO_2 photocatalytic reactor. *J. Colloid Interface Sci.* **2006**, *295*, 159–164. [CrossRef] [PubMed]
53. Liu, Y.; Liu, Y.; Xu, Y.; He, Q.; Yin, R.; Sun, P.; Dong, X. Phenanthroline bridging graphitic carbon nitride framework and Fe (II) ions to promote transfer of photogenerated electrons for selective photocatalytic reduction of Nitrophenols. *J. Colloid Interface Sci.* **2022**, *608*, 2088–2099. [CrossRef] [PubMed]
54. Lu, L.; Li, J.; Ng, D.H.; Yang, P.; Song, P.; Zuo, M. Synthesis of novel hierarchically porous Fe_3O_4@MgAl–LDH magnetic microspheres and its superb adsorption properties of dye from water. *J. Ind. Eng. Chem.* **2017**, *46*, 315–323. [CrossRef]
55. González, M.; Pavlovic, I.; Rojas-Delgado, R.; Barriga, C. Removal of Cu^{2+}, Pb^{2+} and Cd^{2+} by layered double hydroxide–humate hybrid. Sorbate and sorbent comparative studies. *Chem. Eng. J.* **2014**, *254*, 605–611. [CrossRef]
56. Baran, W.; Adamek, E.; Makowski, A. The influence of selected parameters on the photocatalytic degradation of azo-dyes in the presence of TiO_2 aqueous suspension. *Chem. Eng. J.* **2008**, *145*, 242–248. [CrossRef]
57. Shah, R.K. Efficient photocatalytic degradation of methyl orange dye using facilely synthesized α-Fe_2O_3 nanoparticles. *Arab. J. Chem.* **2023**, *16*, 104444. [CrossRef]
58. Nyachhyon, A.R.; Neupane, G. Photocatalytical degradation of Methyl Orange using laboratory prepared Copper Oxide photocatalyst. *Sci. World* **2024**, *17*, 106–113. [CrossRef]
59. Ni, Z.-M.; Xia, S.-J.; Wang, L.-G.; Xing, F.-F.; Pan, G.-X. Treatment of methyl orange by calcined layered double hydroxides in aqueous solution: Adsorption property and kinetic studies. *J. Colloid Interface Sci.* **2007**, *316*, 284–291. [CrossRef]
60. Zhao, X.; Wang, K.; Gao, Z.; Gao, H.; Xie, Z.; Du, X.; Huang, H. Reversing the dye adsorption and separation performance of metal–organic frameworks via introduction of− SO_3H groups. *Ind. Eng. Chem. Res.* **2017**, *56*, 4496–4501. [CrossRef]
61. Ai, L.; Zhang, C.; Meng, L. Adsorption of methyl orange from aqueous solution on hydrothermal synthesized Mg–Al layered double hydroxide. *J. Chem. Eng. Data* **2011**, *56*, 4217–4225. [CrossRef]
62. Asfaram, A.; Ghaedi, M.; Hajati, S.; Rezaeinejad, M.; Goudarzi, A.; Purkait, M.K. Rapid removal of Auramine-O and Methylene blue by ZnS: Cu nanoparticles loaded on activated carbon: A response surface methodology approach. *J. Taiwan Inst. Chem. Eng.* **2015**, *53*, 80–91. [CrossRef]
63. Bulut, Y.; Aydın, H. A kinetics and thermodynamics study of methylene blue adsorption on wheat shells. *Desalination* **2006**, *194*, 259–267. [CrossRef]
64. Han, R.; Zhang, J.; Han, P.; Wang, Y.; Zhao, Z.; Tang, M. Study of equilibrium, kinetic and thermodynamic parameters about methylene blue adsorption onto natural zeolite. *Chem. Eng. J.* **2009**, *145*, 496–504. [CrossRef]

65. Rashed, S.H.; Abd-Elhamid, A.; Abdalkarim, S.Y.H.; El-Sayed, R.H.; El-Bardan, A.A.; Soliman, H.M.; Nayl, A. Preparation and characterization of layered-double hydroxides decorated on graphene oxide for dye removal from aqueous solution. *J. Mater. Res. Technol.* **2022**, *17*, 2782–2795. [CrossRef]
66. González, A.S.; Martínez, S.S. Study of the sonophotocatalytic degradation of basic blue 9 industrial textile dye over slurry titanium dioxide and influencing factors. *Ultrason. Sonochem.* **2008**, *15*, 1038–1042. [CrossRef]
67. Saquib, M.; Tariq, M.A.; Haque, M.; Muneer, M.J. Photocatalytic degradation of disperse blue 1 using UV/TiO_2/H_2O_2 process. *J. Environ. Manag.* **2008**, *88*, 300–306. [CrossRef]
68. Ahmed, S.N.; Haider, W. Heterogeneous photocatalysis and its potential applications in water and wastewater treatment: A review. *Nanotechnology* **2018**, *29*, 342001. [CrossRef]
69. Balakrishnan, A.; Chinthala, M. Comprehensive review on advanced reusability of g-C_3N_4 based photocatalysts for the removal of organic pollutants. *Chemosphere* **2022**, *297*, 134190. [CrossRef]
70. Bisaria, K.; Sinha, S.; Singh, R.; Iqbal, H.M. Recent advances in structural modifications of photo-catalysts for organic pollutants degradation–a comprehensive review. *Chemosphere* **2021**, *284*, 131263. [CrossRef]
71. Crepaldi, E.L.; Tronto, J.; Cardoso, L.P.; Valim, J.B. Sorption of terephthalate anions by calcined and uncalcined hydrotalcite-like compounds. *Colloids Surf. A Physicochem. Eng. Asp.* **2002**, *211*, 103–114. [CrossRef]
72. Zhu, M.-X.; Li, Y.-P.; Xie, M.; Xin, H.-Z. Sorption of an anionic dye by uncalcined and calcined layered double hydroxides: A case study. *J. Hazard. Mater.* **2005**, *120*, 163–171. [CrossRef] [PubMed]
73. Hadjltaief, H.B.; Zina, M.B.; Galvez, M.E.; Da Costa, P. Photocatalytic degradation of methyl green dye in aqueous solution over natural clay-supported ZnO–TiO_2 catalysts. *J. Photochem. Photobiol. A Chem.* **2016**, *315*, 25–33. [CrossRef]
74. Dhatwalia, J.; Kumari, A.; Chauhan, A.; Mansi, K.; Thakur, S.; Saini, R.V.; Guleria, I.; Lal, S.; Kumar, A.; Batoo, K.M.; et al. *Rubus ellipticus* Sm. Fruit extract mediated zinc oxide nanoparticles: A green approach for dye degradation and biomedical applications. *Materials* **2022**, *15*, 3470. [CrossRef]
75. Mani, S.K.; Saroja, M.; Venkatachalam, M.; Rajamanickam, T.J. Antimicrobial activity and photocatalytic degradation properties of zinc sulfide nanoparticles synthesized by using plant extracts. *J. Nanostruct.* **2018**, *8*, 107–118.
76. Tavares, T.D.; Antunes, J.C.; Padrão, J.; Ribeiro, A.I.; Zille, A.; Amorim, M.T.P.; Ferreira, F.; Felgueiras, H.P. Activity of specialized biomolecules against gram-positive and gram-negative bacteria. *Antibiotics* **2020**, *9*, 314. [CrossRef]
77. Monash, P.; Pugazhenthi, G. Utilization of calcined Ni-Al layered double hydroxide (LDH) as an Adsorbent for removal of methyl orange dye from aqueous solution. *Environ. Prog. Sustain. Energy* **2014**, *33*, 154–159. [CrossRef]
78. Javed, T.; Thumma, A.; Uddin, A.N.; Akhter, R.; Babar Taj, M.; Zafar, S.; Mahmood Baig, M.; Shoaib Ahmad Shah, S.; Wasim, M.; Amin Abid, M. Batch adsorption study of Congo Red dye using unmodified Azadirachta indica leaves: Isotherms and kinetics. *Water Pract. Technol.* **2024**, *19*, 546–566. [CrossRef]
79. Urooj, H.; Javed, T.; Taj, M.B.; Nouman Haider, M. Adsorption of crystal violet dye from wastewater on Phyllanthus emblica fruit (PEF) powder: Kinetic and thermodynamic. *Int. J. Environ. Anal. Chem.* **2023**, 1–26. [CrossRef]
80. Ikram, M.; Rashid, M.; Haider, A.; Naz, S.; Haider, J.; Raza, A.; Ansar, M.; Uddin, M.K.; Ali, N.M.; Ahmed, S.S. A review of photocatalytic characterization, and environmental cleaning, of metal oxide nanostructured materials. *Sustain. Mater. Technol.* **2021**, *30*, e00343. [CrossRef]
81. Periyasamy, A.P. Recent advances in the remediation of textile-dye-containing wastewater: Prioritizing human health and sustainable wastewater treatment. *Sustainability* **2024**, *16*, 495. [CrossRef]
82. Attar, R.M.; Alkhamis, K.M.; Alsharief, H.H.; Alaysuy, O.; Alrashdi, K.S.; Mattar, H.; Alkhatib, F.; El-Metwaly, N.M. Remarkable photodegradation breakdown cost, antimicrobial activity, photocatalytic efficiency, and recycling of SnO_2 quantum dots throughout industrial hazardous pollutants treatment. *Ceram. Int.* **2024**, *50*, 36194–36209. [CrossRef]
83. Kamal, A.-B.; Hassane, A.M.; An, C.; Deng, Q.; Hu, N.; Abolibda, T.Z.; Altaleb, H.A.; Gomha, S.M.; Selim, M.M.; Shenashen, M.A. Developing a cost-effective and eco-friendly adsorbent/photocatalyst using biomass and urban waste for crystal violet removal and antimicrobial applications. *Biomass Convers. Biorefinery* **2024**, 1–19. [CrossRef]
84. Akhavan, O.; Ghaderi, E. Cu and CuO nanoparticles immobilized by silica thin films as antibacterial materials and photocatalysts. *Surf. Coat. Technol.* **2010**, *205*, 219–223. [CrossRef]
85. Jannesari, M.; Akhavan, O.; Madaah Hosseini, H.R.; Bakhshi, B. Graphene/CuO_2 nanoshuttles with controllable release of oxygen nanobubbles promoting interruption of bacterial respiration. *ACS Appl. Mater. Interfaces* **2020**, *12*, 35813–35825. [CrossRef]